C F bonding in fluorinated N-Doped carbons

Gaixia Zhang, Marie Colin, Xiaohua Yang, Shuhui Sun, Jean-Pol Dodelet, Marc Dubois

C-F bonding in fluorinated N-Doped carbons

Gaixia Zhang,[1] Marie Colin,[2] Xiaohua Yang,[1] Shuhui Sun,[1] Jean-Pol Dodelet[1], Marc Dubois*,[2]

[1] *INRS-Énergie, Matériaux et Télécommunications, 1650 Boulevard Lionel Boulet, Varennes, Québec, J3X 1S2, Canada*

[2] *Université Clermont Auvergne, CNRS, SIGMA Clermont, Institut de Chimie de Clermont-Ferrand, F-63000 Clermont-Ferrand, France*

*Corresponding author. Tel: 0033473407105. E-mail: marc.dubois@uca.fr (Marc Dubois)

Abstract

Porous carbons are used in various applications for energy storage. Nitrogen doping of these carbons modifies their electrochemical and chemical properties and co-doping them with fluorine atoms, appears as a promising route to further tailor their physical and chemical properties. The present paper focuses on the gas/solid fluorination with molecular fluorine (F_2) of various types of N-doped porous carbons. The consequences of the fluorination on the porosity of these materials were studied as well as their C-F bonding type. Mild conditions avoid a huge decomposition in F_2 gas of these materials and a drastic decrease of their specific surface area. Micropores, which are hosting most of the FeNx catalytic sites, are the most affected by fluorination, and a new N1s XPS peak assigned to pyridinic-N---C-F has been identified, coinciding with that of the XPS binding energy of N1s in FeNx. However, molecular fluorine did not react directly with nitrogen atoms in these materials, whatever their type since no N-F containing volatile products were evolved during the treatment. Finally, a dual C-F bonding, characterized by the coexistence of C-F bonds with weakened covalence and covalent C-F, is evidenced in all fluorinated N-doped porous carbons.

1. Introduction

Owing to their unique structures, excellent physicochemical stability, numerous synthesis routes and low-cost [1,2,3,4,5] , carbons doped with heteroatoms such as nitrogen atoms are extensively studied for their changes in the local density of states, inducing charge polarization in close proximity to N dopants [6,7] as well as structural defects. It has been demonstrated that nitrogen doping is also an efficient method to enhance the electrical conductivity of carbons, enlarge their interlayer spacing and increase the number of active sites for multilayer graphene. N-doping also results in activity for metal-free carbon-based oxygen and hydrogen electrocatalysts [8]. All those changes offer the possibility of tailoring the electrochemical properties for oxygen reduction in polymer electrolyte

membrane (PEM) fuel cells, hydrogen and oxygen evolution from water [9,10,11,12,13], carbon dioxide reduction [14], environmental pollutants removal, lithium-ion storage [15,16,17], lithium-sulfur batteries [18,19,20,21], supercapacitors [22,23,24,25,26], adsorption and sensing [27].

Fluorine doping acts also on the electronic properties of metal-free carbons modifying, for instance, the optical properties of carbon dots [28]. A few works also report co-doping of N and F atoms, e.g. of carbon dots as contrast agents for magnetic resonance imaging [29] or of porous carbon for oxygen reduction reaction (ORR) catalyst [30]. A maximum C−C bond polarization, charge redistribution, and high spin densities in the carbon matrices are achieved with the simultaneous presence of N, in the form of pyridinic-N, pyrrolic-N, graphitic-N, active species, and of F in the form of C−F ionic and C---F with weakened covalence, ie. semi-ionic, active forms. A synergistic enhancement of the activity has been reported for N and F-doped ORR metal-free catalysts [28] as well as for F and N bifunctional improved oxygen electrocatalysts for regenerative fuel cells and metal-air batteries [31]. Due to the presence of fluorine and the resulting large difference of electronegativity between fluorine and carbon, N and F co-doped graphene quantum dots exhibited enhanced electrochemical reaction property and stability for full water splitting and supercapacitor [32]. N and F co-doping of reduced graphene oxide favors ORR stability [33]. High sodium ion storage capacity, fast transfer kinetics and stable cycling were achieved with F and N co-doped carbons, thanks to particular structural and morphological features [34]. For both single or dual dopings, the fluorination was performed using mild conditions, i.e. a solvothermal process using an aromatic F-bearing moiety as the F source [28], pyrolyzing a mixture of carbon black, polytetrafluoroethylene (PTFE) and melamine [31], or a hydrothermal process with trifluoroacetic acid or NH_4F [33, 30], one-pot pyrolysis of PTFE, a nitrogen containing resin, and potassium hydroxide, covalent grafting of the 4-(trifluoromethyl) phenyl diazonium salt [29]. A two-step synthesis was carried out for graphene quantum dots with fluorination of CVD precursor using dielectric barrier discharge plasma at atmospheric pressure [32].

Fluorination of metal-based ORR catalysts has also been reported. For instance, fluorination of Pt/C catalysts for PEM fuel cell with atomic fluorine resulted in disorganized Pt becoming quite inactive towards ORR [35]. The fluorine content gas acted negatively on the stability in fuel cells. Beneficial effect was observed when more C-F bonds were formed with F_2 in disordered carbons [36]. For Pt/C it was concluded that Pt contributed to the fluorination mechanism and that the treatment increased the pore size and decreased the specific surface area of the carbon structure [35]. As far as Fe/N/C ORR based catalysts are concerned, the situation is more complex. Indeed, fluorination of some Fe/N/C catalysts may render it superhydrophobic with rather stable currents [29]. On the contrary,

for other Fe/N/C catalysts, all Fe-based catalytic sites were poisoned during fluorination with F_2, even after 2 min of treatment [37].

The present work aims to investigate the C-F bonding for various types of N-doped carbons, i.e. conventional N-doped BP, where BP is a Black Pearls carbon black, N-doped pyrolyzed metal organic framework (MOF), and N-doped porous carbon with FeNx catalytic sites. The multiscale characterization of those resulting fluorinated N-doped carbons will establish the nature of C-F bonds. The consequences of fluorination on porosity will be studied, as well as the C-F bonding and the N-doped carbon thermal stability. The comparisons of the physical and chemical properties for, on the one hand, BP and N-doped BP and, on the other hand, pyrolyzed N-doped carbons deriving from MOF, with or without FeNx ORR catalytic sites, will demonstrate what is the influence of the N atoms and of the FeNx catalytic sites on the fluorination of these materials. The collected data on these various fluorinated N-doped carbons will certainly be useful to extend their uses for energy conversion and storage.

2. Experimental

2.1 Materials

The carbon black named Black Pearls 2000 (BP2000, denoted here BP) has been kindly provided by Cabot Corp. Whereas carbon blacks contain on their surface CO, OH, and COC functionalities with both basic and acidic carbons [38], BP has rather a more acidic than basic character [39]. BP is a disorganized carbon with particles on the nanometer scale that agglomerate to form larger aggregates with high nanoscale porosity and a very high surface area (1039 $m^2.g^{-1}$). N-doped Black Pearls (BP-N) was obtained by first heat-treating BP in argon at 1050 °C for 1 h, then in NH_3 at 950 °C for 45 min, resulting in a mass loss of 50 % [40].

N-doping was also performed during the pyrolysis of a Zn imidazolate metal organic framework MOF (labeled ZIF-8 or Basolite™ Z1200 from Aldrich). An amount of 1600 mg of MOF was mixed in 100 mL ethanol and 50 mL deionized water. The mixture was stirred for about 2 h at room temperature. Then it was heated to 60-80 °C until a thick slurry of about 50 mL was left. The slurry was placed in a drying oven at 95 °C and in air, where it was left overnight. The resulting dry powder was transferred under N_2 in a 65 cm^3 steel vial containing 20 chrome-steel balls of 0.25 inch diameter. After sealing the vial under N_2, it was placed in a planetary ballmiller (Pulverisette 7, Fritsch) for 3 h at 400 rpm. After ballmilling, two pyrolysis steps were performed: (i) a pyrolysis under Ar at 1050 °C for 1 h until

a mass loss of about 70 % was obtained, and (ii) another pyrolysis under NH_3 at 950 °C for 5 min until a subsequent mass loss of about 20 % was obtained [41].

A N-doped carbon with FeNx catalyst (denoted NC) was synthesized according to the optimized conditions described in the reference [42]. ZIF-8 (from Aldrich) was used as N-precursor, with 1,10-phenanthroline (another N-precursor and iron complexing agent, from Aldrich: purity ≥ 99%), and iron(II) acetate (the Fe-precursor from Aldrich: purity 95%). The optimum nominal iron loading was 1 wt %.

2.2 Fluorination

Whatever the carbon or the catalyst, fluorination was carried using a dynamic mode with a flux of molecular fluorine gas (F_2, less than 0.1 vol.% of admixtures, mainly oxygen), into an opened passivated nickel reactor (covered with NiF_2). Before fluorination, around 100 mg of samples were outgassed overnight at 120 °C under primary vacuum (10^{-3} mbar), in order to eliminate adsorbed molecules from their surface. This pre-treatment is of primary importance for high surface material because adsorbed water molecules would lead to the formation of HF during exposure to F_2. HF catalyzes fluorination and inhomogeneous reaction may occur. Fluorination was then performed at room temperature under a 50 mL min^{-1} flux of F_2/N_2 (1:1 in volume, Nitrogen was of 99.999% purity) at atmospheric pressure. After fluorination, a nitrogen purge of the reactor replaced the residual molecular fluorine and possible decomposition products like NF_3, CF_4 and C_2F_6. The resulting materials were outgassed at 150 °C for 2 h under primary vacuum (10^{-3} mbar), in order to eliminate the weakest C-F bonds and adsorbed molecules like F_2, HF, NF_3, CF_4, and C_2F_6.

The samples are denoted Fduration-BP (e.g., F20min-BP), Fduration-BP-N, Fduration-MOF and Fduration-NC according to the treatment duration for BP, BP-N, MOF and NC as carbons or Fe-based catalyst, respectively.

2.3 Characterization

FTIR spectra recorded in the Attenuated total reflection (ATR) mode (with diamond crystal) were measured with a Nicolet 5700 FTIR spectrometer. All spectra were measured at 4 cm^{-1} resolution and 512 scans were taken for each spectrum.

Multinuclear NMR measurements were performed using a BRUCKER AVANCE spectrometer, with working frequencies for ^{13}C, ^{1}H and ^{19}F of 73.4, 300.1 and 282.2 MHz, respectively. Magic angle spinning (MAS) probes (Bruker) operating with a 4 or 2.5 mm rotors were used. For MAS spectra, a simple sequence was performed with a single $\pi/2$ pulse length of 4 and 3.5 µs for ^{19}F and ^{13}C,

respectively. A cross polarization (CP)/MAS NMR probe (Bruker) with proton decoupling on a 4 mm rotor was used. ^{13}C chemical shifts were externally referenced to tetramethylsilane (TMS). ^{19}F chemical shifts were referenced with respect to $CFCl_3$.

A confocal Raman system, model inVia from Renishaw, using a 532 nm laser excitation, was used for Raman analysis. The irradiation power was set in order to avoid damage to the sample surface and maximize the emission signal intensity. The spectra reported here are corrected for their background.

X-ray photoelectron spectroscopy (XPS). Surface elemental analysis was measured by XPS using a VG ESCALAB 200i instrument. Due to the lower conductivity of the fluorine treated samples, the twin Al Kα line (1486.6 eV) was chosen as the X-ray source for all the XPS measurements. This is because, as the X-rays pass through the aluminum window on the nose of these sources, a flood of low-energy electrons is produced that effectively and automatically compensates for most charge uniformity effects. The peak energies were calibrated by placing the graphite C1s peak at 284.6 eV. CasaXPS software was used to fit the spectra and calculate the quantification of C, N, O, F, Fe and Zn elements. The spectra were fitted with mixed Gaussian-Lorentzian component profiles after a Shirley background subtraction.

Thermogravimetric analysis (TGA) was conducted using Thermo-Gravimetric Thermal Analyzer (TGA Q500 from TA instruments). All measurements were carried out under He with a flow rate of 100 $mL.min^{-1}$. The samples were equilibrated at 30°C, then heated to 1000 °C at a ramp rate of 10 $°C.min^{1}$. A cylindrical platinum crucible was used for analyzing these samples. Before each experiment, in order to remove impurities, the platinum crucible was first cleaned by sonication, then heated with a torch until it became red hot (>1100 °C).

N_2-sorption isotherms at 77 K were recorded with a Quantachrome Autosorb-1 instrument. The pore size distribution was analyzed by the Autosorb-1 software, using the quenched solid density functional theory (QSDFT) and assuming pores with a slit-like structure.

3. Results and discussion

3.1 Chemical homogeneity of the fluorinated materials

Since NMR (bulk) and XPS (surface) are two techniques probing different scales in material characterization, the comparison of the fluorination rates obtained by these two techniques allows the homogeneity of the material to be evaluated. The fit of the ^{13}C NMR spectra gives the effective fluorine content with accuracy equal to 0.02 [43]. The fluorination rate may be expressed as a F/C

atomic ratio or as x in CF_x composition. For most of the cases, a good accordance is found between F/C values obtained by XPS and NMR (Tab. 1). Moreover, the weight uptake due to fluorination, i.e. covalent grafting of F atoms, gives an approximate F/C ratio. This concordance evidences that no huge decomposition of the carbon or the catalyst support into CF_4 or C_2F_4 gases occurred. Significant differences are, however, observed for longer fluorination durations, i.e., for F1h-BP-N, F/C = 0.42 is obtained from XPS, while F/C = 0.30 is deduced from NMR. For those conditions, the surface F/C measured by XPS always exhibits a higher fluorine content than F/C values measured by NMR for the bulk of the samples. A perfluorination of the surface with the formation of CF_2 groups may explain such differences. Moreover, when decomposition in F_2 gas occurs, CF_3 groups are formed. A particular attention will be devoted to those groups considering NMR and XPS data.

Still in Tab. 1, it is to note that the oxygen content increases after fluorination except for BP-N. Some C-C and C-O bonds will be broken during the fluorination processes, forming dangling bonds (radicals), which will react with oxygen and moisture upon exposure to air. Similar process has been observed for the fluorination of polymers [44,45]. When the initial O relative content is already high, as for BP-N, then fluorination results in the conversion of oxygenated groups into C-F bonds [46,47]. Neither N nor Fe contents are affected by the fluorination, their values remaining nearly constant. Since the resulting fluorine contents are similar after a given fluorination duration, the presence of catalytic FeNx sites or of nitrogen dopants does not seem to influence the reactivity of the carbon-based materials towards F_2 gas.

3.2 C and C-F bonding

Because of the disordered nature of the starting materials, Raman spectra exhibit a high D band (see Fig. SI-1 in supplementary information for the representative example of NC), the ratio of the integrated D (Disorder band around 1300 cm^{-1}) to G (Graphitic band around 1600 cm^{-1}) bands is then initially high. Consequently, fluorination does not affect significantly this ratio. Structural changes obtained from Raman or X-ray diffraction spectra will not be discussed further.

FTIR spectroscopy gives a first insight into the C-F bonding (Fig. 1a). Whatever the fluorinated sample, two vibration bands are observed in the 800-1450 cm^{-1} range. The higher the bond strength (covalence), the higher the wavenumber [48,49,50,51,52]. The bands at 1220 and 1110 cm^{-1} are assigned respectively to covalent C-F bonds (noted C-F) and C-F bonds with weakened covalence (noted C---F); the weakening of the covalent bond strength (or hyperconjugation, as reported by Sato [53]) results from the presence of non-fluorinated carbon atoms, still with sp^2 hybridization, in the

neighborhood of C-F bonds (involving sp^3 C). In other words, the deconvolution of FTIR spectra in the 850-1450 cm^{-1} range allows the relative contents of C-F/C---F to be estimated (see Fig. 2). Whereas one expected an increase of the covalence bond strength (by a decrease of the hyperconjugation) with increasing fluorine content (since the relative content of non-fluorinated sp^2 C decreases), the opposite is observed for BP and BP-N. Indeed, for BP and BP-N, the relative content of weakened covalence bonds (C---F) increases with the fluorination duration (or with the increase of the F/C value), e.g. the integrated surfaces of C---F (from FTIR) for the BP series are 55, 64 and 73 % after 20 min, 1 h and 12 h, respectively (Fig. 2b), and the F/C values (from XPS) for the same samples are 0.12, 0.24 and 0.35, respectively (Tab. 1). A possible explanation of this behavior is a two-step reaction mechanism: first, the fluorination of the most reactive sites (mainly the oxygenated sites) leads to the formation of covalent C-F bonds by substitution of O by F [54]. Bonds with weakened covalence (C---F) are then formed by conversion of sp^2 carbons into sp^3 ones after fluorination and their relative content increases with the fluorination duration. For NC and MOF, the relative content of C-F bonds with weakened covalence (C---F) bonds always remains around 60% (Fig. 2b) regardless of the fluorine content and the fluorination time. It will be shown later on that this behavior is related to the type of pores found in NC and MOF, rather than to the fluorination extent as noticed for BP and BP-N.

The value of 700-750 cm^{-1} for CF_2 in Fig. 1 instead of 1000 cm^{-1} usually recorded for fluorinated carbons may be explained by the disordered character of our samples. As a matter of fact, when the crystalline order of fluorinated carbons decreases, the wavenumber of CF_2 vibration band shifts towards low values [55]. No band is related to N-F vibration. The most intense band for NF_3 is expected at 840-960 cm^{-1} [56].

The predominance of C---F bonds with weakened covalence is confirmed by NMR according first to the ^{19}F chemical shift δ_{19F} (Fig. 3a to 6a). Indeed, the weakening of the C-F covalence results in a shift of δ_{19F} values towards around -150 ppm of a peak usually recorded at -190 ppm for strong covalent C-F bonds [48,51,57,58,59,60,61,62]. For the lowest fluorine content (F/C = 0.05 in Fig. 3a, 10 min), the ^{19}F-^{19}F homonuclear dipolar coupling is still low because of the dilution of F atoms and several separated narrow bands appear. Such coupling results in band overlapping when the fluorination time increases. Even a MAS spinning rate of 30 kHz is not sufficient enough to reduce this coupling as evidenced by the case of F-1h-BP-N (Fig. 4a, upper curve). Whatever are the sample and fluorine content, the amounts of CF_2 groups (with δ_{19F} around -120 ppm) and CF_3 groups (with δ_{19F} between -60 to -80 ppm) in Figs 3a to 5a are low in accordance with a weak decomposition during fluorination (as discussed regarding the F contents from XPS, NMR and weight uptake). As a matter of fact, especially for disordered carbonaceous materials, an over-fluorination of the graphene layers results

in the release of CF_4 and C_2F_6 gases, graphene layer disruptions, and an increase in the number of layer edges. Those edges are then perfluorinated with CF_2 and CF_3 groups. The number of spinning sidebands for F-NC in Fig. 6a is explained by the presence of paramagnetic FeNx sites in the catalysts.

$^{19}F \rightarrow {}^{13}C$ cross-polarization favors the observation of CF_2 groups with a chemical shift of 110 ppm. This band is of very low intensity regardless of the F content in accordance with an absence of decomposition for the fluorinated carbon (Fig. 3b to 6b). When such a process occurs, defects are formed in the carbon lattice and sheet edges are perfluorinated with CF_2 groups. The higher the disorder induced, the higher the CF_2 content [46,47,63]. The two main bands in $^{19}F \rightarrow {}^{13}C$ CP-MAS spectra (Fig. 3b-6b) are assigned to C-F bonds (with δ_{13C} = 80 ppm, for C-F in these figures, where C-F defines a carbon atom with a bond with F), and sp^2 C where C-C-F defines a carbon atom in close vicinity with the C-F bond; the interaction of a sp^2 C and its neighbor C-F bond results in a chemical shift of 130 ppm, which is larger than the value of δ_{13C} =120 ppm found for pure graphite. With cross-polarization, only sp^2 C atoms in the neighboring C-F bonds appear; their chemical shift is similar whatever the F content is. On the contrary, when all carbons are measured with simple MAS (Fig. 3c-6c), the position of the (C-C-F) band shifts towards a higher δ_{13C} value (from 120 to 130 ppm) when F/C increases and the ratio C---F/C-F increases for the BP and the BP-N series. For fluorinated NC, the position does not change (δ_{13C} = 130 ppm) because the ratio C---F/C-F remains constant upon fluorination (Fig. 2b). The ratio $S_{C\text{-}F}/(S_{C\text{-}F}+S_{C\text{-}C\text{-}F})$ is equal to F/C or x in CF_x ($S_{C\text{-}F}$ and $S_{C\text{-}C\text{-}F}$ are the integrated surface of the corresponding bands). The values are reported as F/C (NMR) in Tabs. 1 and 2. The chemical shift for C-F is 80 ppm, which is lower than for covalent C-F (84-90 ppm) [57,58,59,60,61,62], gives an additional evidence of a weakening of the C-F bonding. When different zones are formed during the fluorination, ^{13}C NMR spectra exhibit different bands and their linewidths differ too[62]. It is not the case for the present sample and fluorination is homogenous, fluorine atoms being well dispersed onto the whole surface regardless of the sample. Fluorination occurred progressively without huge decomposition and involved the whole carbon surface.

3.3 F and C-F bonding

The F1s XPS spectra for the BP series are presented in Fig. 7c and their deconvolutions appear in Fig. SI-2. For the BP-N series, the MOF and the NC series, the F1s XPS spectra and their deconvolutions are shown in Fig. 8c, 9c, and Fig. SI-3a and c, respectively. All F1s spectra were deconvoluted into five peaks denoted: C---F, C-F, CF_2, M-F_2, and M-F (or Fe-F_2 and Fe-F in the case of NC), where M is a metallic impurity present in the raw materials, e.g. Zn in MOF, or introduced during the fluorination, e.g. NiF_2 from the passivated reactor). The numerical results of these deconvolutions were summarized in Tabs. 3 and 4. According to the literature [46,47,64,65,66,67,68,69], three peaks

were assigned to fluorinated carbons: the first at binding energy (BE) of ~ 686.8 eV is unambiguously assigned to C---F bonds. It is the main peak in the four analyzed series. The peak at ~ 688.3 eV is attributed to covalent C-F and the one at ~ 690.0 eV is related to CF_2 groups. The CF_2 content is very low for all the samples which is well consistent with the NMR results mentioned previously. The other two peaks at low BE (M-F_2 and M-F in the BP, BP-N, and MOF series) are also necessary to fit the experimental F1s spectra. They are assigned to M-F (~ 684.1 eV) and M-F_2 (~ 685.4 eV) [70,71]. In the case of the NC series, it is obvious that F_2 also reacted with iron in the NC catalyst to form fluorides, as the contents of the two low BE peaks in the fluorinated NC series are much higher than those of the other series.

Alike FTIR measurements already presented in Fig. 2, XPS measurements also enable to evaluate the relative C---F content in the four series of fluorinated materials. The following conclusions were reached from the comparison of the FTIR and XPS results: (i) On the one hand, the relative C---F contents in fluorinated MOF and NC series deduced by XPS are in reasonable agreement with the relative C---F contents deduced by FTIR for the same materials. For instance, the (FTIR) relative C---F content in F20min-NC is 62% (Fig. 2b) while that deduced for XPS is 59.9% (Tab. 4); (ii) On the other hand, the relative C---F contents in fluorinated BP or BP-N series deduced by XPS disagree with that deduced by FTIR from the same materials. For instance, the C---F relative content in F20min-BP is 55% (Fig. 2b), while it is 86.1% when it is deduced by XPS (Tab. 3). The difference in C---F relative contents between these two techniques decreases, however, when the fluorination time increases. For instance, the C---F relative content in F12h-BP is 73% (FTIR, Tab. 2b), while it is now 86.5% when it is measured by XPS (Tab. 3). This difference may arise from the porosity of these materials (see Tab. 2). Fluorinated NC and MOF exhibit lower surfaces in comparison with the other fluorinated samples. The higher surface may favor a dilution of the C-F bonds and then the hyperconjugation. As XPS probes the surface of the materials, it reveals this trend.

The C1s XPS spectra for the BP series are presented in Fig. 7a and their deconvolutions appear in Figs. SI-3b and 3d. For the BP-N series, the MOF and the NC series, the C1s XPS spectra and their deconvolutions are shown in Fig. 8a to 8c, Fig. 9a and c, and Fig. SI-3b and 3d, respectively. The content of each assigned carbons for all series is given in Tab. 5. C1s XPS spectra are normalized to the same C1s areal intensity, meaning that each spectrum has the same area under the C1s envelope. C1s XPS spectrum of porous carbons before fluorination is deconvoluted into four or five components depending on the presence of N atoms [72,73]. The components are: C1 assigned to an undamaged carbon at the BE of 284.6 eV; C2 assigned either to a corresponding damaged alternant carbon (N-doped carbons) or to a carbon involved in a C-OH bond at 286.1 eV; C3 assigned either to a

Csp^3 free radical defect or to a carbon involved in a C=O bond at 287.6 eV; C4 assigned to a carbon involved in a COOH functionality at 289.6 eV; C5 assigned to a C1s $\pi^* \leftarrow \pi$ shake-up satellite at 291.4 eV. Only for NC, an additional component is considered (C6), at 282.5 eV, assigned to carbon in iron carbide. The XPS contents of each assigned carbons are given in Tab. 5.

Fluorination results both in the losses of oxygenated groups and in the formation of C-F bonds (listed in Tab. 3). Some components exhibit similar BEs (C-OH and C---F, COOH and C-F) which makes the assignment complex. We assumed that the low C=O and C-OH contributions disappeared. Whatever the sample, the drastic decrease of C1 after fluorination and the increase of the C3 and C4 relative components (illustrated in Fig. 7b) are related to the formation of C-F bonds. C2 ($\sim$ 286.1 eV) decreased for the shortest fluorination duration and then increased with the treatment time; it is then also assigned to a carbon atom (C*) next to another carbon atom bound to fluorine (C*-C-F), while C3 and C4 at $\sim$ 287.6 and $\sim$ 289.6 eV are related to C*---F and C*-F, respectively.

3.4 N and C-F bonding

Fig. 10 presents the N1s XPS spectra of the MOF series. Due to their very low N content (see Tab. 1), the N1s spectra of the BP-N samples displayed in Fig. SI-4 could not be deconvoluted. All N1s spectra of the MOF series were deconvoluted into the usual four peaks, i.e. pyridinic N (BE of 398.3-398.8 eV), pyrrolic N (or hydrogenated pyridinic) (400.6-401.3 eV), graphitic N (402.1-403 eV), and oxidized N (403.6 eV) [74] Table 6 gives the relative content of each N1s component.

Looking to Fig. 10a, it is obvious that the shape of the MOF N1s spectrum drastically changes after fluorination to become F20min-MOF. Figs. 10b and c are displaying the deconvolutions of N1s for MOF and F20min-MOF, respectively. It was possible to deconvolute the MOF N1s XPS spectrum into the usual four peaks mentioned above, all of them having a width (FWHM) of 1.5 eV. An additional peak was, however, necessary to fit the N1s spectrum of F20min-MOF. This peak (dotted black line in Fig. 10c) has the following characteristics: a binding energy of 399.7 eV and a FWHM of 1.5 eV. We are proposing to assign it to what we have named: pyridinic N---C-F, which would be a pyridinic N on the edge of a graphene plane with a fluorine atom replacing a terminal hydrogen on a carbon in ortho position vs the pyridinic N (see the structural illustration, in Fig. 10, of the various nitrogen atoms substituting for carbon in a graphene layer). This new peak and its assignment would explain the drastic decrease of the large pyridinic N1s MOF peak compared with that of F20min-MOF and the disappearance for F20min-MOF (Fig. 10c) of the valley between the pyridinic and pyrrolic peaks seen for MOF in Fig. 10b.

Here, one may argue that instead of assigning the new peak to pyridinic N---C-F, one might assign it to pyridinic N-F, an equivalent to hydrogenated pyridinic N (pyridinic N-H) where -H would have been replaced by -F (in pyridinic N-F). The BE of hydrogenated pyridinic is known to be at least in the same range than that of pyrrolic N (400.6 – 401.3 eV) [74]. Given the more electronegative character of F vs H, a BE even higher than that assigned to hydrogenated pyridinic N would be expected for pyridinic N-F. This is not what is observed in the deconvolution since the new added peak (dotted black line in Fig. 10c has a BE of 399.7 eV. Furthermore, no N-H characteristic vibration has been observed in the FTIR spectrum of MOF (nor in the spectrum of any other fluorinated material analyzed in this work).

Let us now analyze the N1s spectra and their deconvolutions for the NC and fluorinated NC catalysts, which are given in Fig. 11 and Fig. SI-5. Fig. 11a displays all N1s XPS spectra for NC and Fxmin-NC, where x = 2, 5, and 20 min of fluorination. Alike for MOF in Fig. 10a, one sees that, in Fig. 11a, even 2 min of fluorination greatly modifies the shape of the N1s spectrum. Fig. 11b presents the deconvolution of the N1s spectrum for NC. Here, besides the usual pyridinic, pyrrolic, graphitic, and Noxide components already mentioned for the MOF series, two additional peaks were also used for the N1s spectra of the NC series, i.e. FeNx (FeN_4) (BE of 399.5-399.8 eV [74]) and a small peak assigned to iron nitride (BE of 397.1eV [75]). Table 6 gives the relative content of each N1s component.

Note that the binding energy of the FeNx peak in Fig. 11b is 399.7 eV, which is exactly the same value that binding energy already assigned to the pyridinic N---C-F peak in the deconvolution of F20min-MOF (Fig. 10c). This enables us now to understand the deconvolution of all fluorinated NC materials, as it is proposed for Figs 11c and d, as well as for all deconvolutions of Fig. SI-5, that the large peak observed at 399.7 eV (dotted blue line) in these figures has two components: the first one, FeNx (FeN4) is similar to that seen in Fig. 11b for pristine NC, and the second one, a new contribution of pyridinic N---C-F, resulting from the fluorination of the NC catalyst. This interpretation not only explains the shape of the N1s peaks for all fluorinated materials of the NC series, but also that of the N1s spectrum of Fig. 11d, which was obtained after heat treating F20min-NC at 600°C in Ar. In that case, some if not all the C-F bonds of pyridinic N---C-F were thermally decomposed, returning the nitrogen atom to its pre-fluorination pyridinic N form, and retrieving, therefore, a deconvoluted spectrum quite similar to that of pristine NC (Fig. 11b).

If we like now to be more quantitative in our analysis of the N1s XPS data reported in Table 6, and given the importance of the fluorine content (up to 30.2 at% for F20min-MOF and 26.0 at% for F20min-NC, see Tab. 1) vs 0 at% for the unfluorinated MOF, it becomes first necessary to correct the

results of Tab. 6 for the presence of fluorine in F20min-MOF. This is done by multiplying the absolute content of each peak of F20min-MOF by a correction factor, which is the ratio of the carbon content in MOF divided by the carbon content in F20min-MOF. Here the correction factor f = 89.9 / 60.6 = 1.48; see C-contents for MOF and F20min-MOF in Tab. 1. The C-normalized absolute (C-norm-abs-) N1s contents for each peak of F20min-MOF are given (in Italic) in Tab. 6. Of course, the correction factor for unfluorinated MOF is f = 1.0, and the absolute content for each peak of MOF listed in Tab. 6 is the same as its C-norm-abs-content. A similar correction was also performed for F20min-NC vs NC (see Tab. 6) and for the comparison of F20min-NC and F20min-NC_600C (see Table SI-2).

Let us now discuss the results presented for the MOF and NC series in Tab. 6. First, the fluorination of MOF and NC did practically not change the total C-norm-abs-content of N1s. It is 6.5 at% for MOF and 7.0 at% for F20min-MOF. The same observation is also made for NC (total N1s content = 4.9 at%) and for F20min-NC (total C-norm-abs-content = 4.7 at%). One may therefore conclude that, during fluorination, F did not react with N in these materials to yield volatile products.

Second, after fluorination of MOF, there is a 2.3 at% drop of the C-norm-abs-content for pyridinic N (from 3.6 to 1.3 at%), which is compensated by the formation of 1.9 at% of pyridinic N---C-F (from 0 to 1.9 at%), while, after fluorination of NC, there is a 1.0 at% drop of the C-norm-abs-content for pyridinic N (from 1.9 to 0.9 at%), which is compensated by the formation of 0.8 at% of pyridinic N---C-F (from 0.5 to 1.3 at%), assuming that the 0.5 at% content of N atoms engaged in the FeNx catalytic site for NC remains the same after fluorination. This assumption seems to be correct since when F20min-NC is thermally treated at 600°C, the absolute content of FeNx returns to 0.5 at% for F20min-NC_600. If the pyridinic N-content is greatly affected by the fluorination, the variations of the other N atom species seem to remain unaffected, except perhaps for the graphitic N, but the effect, while similar to that observed for pyridinic N becomes, however, minimal for graphitic N. Some graphitic N may indeed be located near the edges of the graphene layers where an adjacent carbon may be fluorinated.

3.5 Thermal stability of C-F bond

Based on the three TGA curves presented in Fig. 12, let us now discuss about the stability of the C-F bonds. All TGA experiments were carried out in He atmosphere up to 1000 °C. Fluorination is responsible for differences between the TGA curves in Figs 12a and 12b, the fluorinated materials being thermally less stable than the unfluorinated ones. Fig. 12c displays this difference in thermal stability in terms of a difference in mass lost by the fluorinated vs unfluorinated NC. There is a first differential mass lost of about 4% between room and 150°C, which is attributable to HF or H_2O in F20min-NC. The slope of the curve changes over 150°C. As the temperature increases, F atoms involved in C---F bonds are expected to be lost first, before F atoms involved in C-F bonds, but no

transition between C---F and C-F is visible on the curve. It means that there is a continuous range of bond energies for C---F and another continuous range of bond energies for C-F.

At 800°C, it seems that practically all carbon-fluorine (and metal-fluorine) bonds are broken. On Fig.12c, y-x = 28%, which is very close to the absolute F1s content of 26 at% deduced by XPS for F20min-NC (Tab. 4). From the same Table, we are also able to obtain a 22.5 at% for the peaks only related to carbon-fluorine bonds. Given that 22.5 at% is 87% of 26 at%, using this value to correct y-x for carbon-fluorine bonds only, one obtains 0.87 (y-x) = 0.87 (28%) = 24% or F/C = 0.24 deduced by TGA.

The F/C value obtained by XPS for F/C = 0.40 for F20min-NC (Tab. 1). When the same correction is applied to this value to take the M/Fe-Fx into account, a value of F/C = 0.40 x 0.87 = 0.35 is obtained by XPS for F20min-NC. Summarizing all these results, F/C = 0.27 (by NMR), 0.35 (by XPS) and 0.24 (by TGA) are obtained for F20min-NC. Their mean value is: F/C = 0.28 ± 0.06.

It is important to note that half of fluorine atoms already disappeared from F20min-NC around 350°C and also that at 600°C, from Fig. 12c, there are only (32-28)/(32-4) = 14% of the fluorine atoms left on F20min-NC as calculated by TGA. This compares well with the values obtained from Tab. 4: 100 x (4.4 /26) = 17% of fluorine atoms left on F20min-NC as calculated by XPS.

The weakening of the C-F covalence may favor the defluorination and then introduce the possibility to tailor the fluorine content by thermal treatment.

3.6 Porosity and the C-F bond

No difference in the fluorination mechanism was found according to the presence of FeNx catalyst or N-doping. Nevertheless, the relative contents of C---F and C-F behave differently for BP, N-BP and NC (see Fig. 2b). C---F content increases for BP and BP-N, whereas it is constant for NC, with the same percentage than fluorinated MOF (around 65% of C---F). Because fluorination is a heterogenous gas/solid reaction, both the type of pores and the specific surface area (SSA) act on the reaction [46,47,63]. Comparison of SSA for raw samples and corrected SSA (calculated for equivalent carbon mass, i.e. corrected for the presence of fluorine) after treatment evidences a decrease, but not a drastic one, with a maximum loss of 40% (Tab. 2). The adsorption isotherms presented in Fig. 13, before and after NC fluorination, have the same shape, but a significant loss of the adsorbed nitrogen volume is observed after fluorination. The mesopore volume V_{meso} (see Tab. 2) does not significantly change during fluorination whatever are the conditions and starting material. On the contrary, the micropore volume decreases with F/C for all the cases, which results in the decrease of both SSA and the total pore volume. MOF and NC are mainly microporous, while BP and N-BP exhibit a mixture of micro and mesopores. For mainly microporous samples, the losses of both pore volume and SSA are maximum even for short fluorination times (see F5min-NC in Tab. 2). A systematic study of porous

carbons with controlled porosity evidenced that, starting from a mesoporous carbonaceous material, the surface decrease was only around twenty percent. The loss of surface was mainly due to a decrease in the micropore volume [46]. In the present study, the same trend is observed. The main differences are due to the microporous character of NC and MOF.

4. Conclusion

Porous carbons displaying different properties such as: 1) N-doped or not, 2) with microporous or with a significant part of mesopores, or 3) with or without FeNx catalytic sites, were fluorinated. Their chemical and physical characterizations allow the following trends of their fluorination to be established: i) Neither N atoms (with a content up to 6.5 at.%) nor FeNx catalytic sites (with a Fe content around 1 at.% from XPS data) act directly on the fluorination mechanism; their atomic contents are too low to change the reaction. ii) No N-F bonds are formed during fluorination (the resulting content is too low to be detected by NMR or FTIR). Moreover, the total N content remains unchanged; iii) if molecular fluorine did not react directly with N in these materials regardless of their type (pyridinic, pyrrolic, hydrogenated pyridinic, graphitic or oxidized) to yield volatile products, fluorination is, however, able to influence the binding energy (BE) of pyridinic N. A new N1s XPS peak, assigned to pyridinic-N---C-F, has indeed been identified with a BE of 399.7 eV coinciding with that of the XPS BE of N1s in FeNx. The binding energy of all other types of nitrogen in these materials is practically not affected by the fluorination. This is important since nitrogen atoms are known to change the local density of states around the Fermi level of N doped carbons; they play a key role in tailoring the electronic and adsorption properties of these materials. iv) All Fe-based catalytic sites were poisoned by reaction with F_2, even after 2 min of fluorination [37]. For improving fuel cell performances, the catalyst sites should be added after fluorination. With this two-step process, enhanced stability may be achieved [35,36]. Using another strategy, the F_2-poisoned NC catalysts may be partially (~ 70%) reactivated by a heat-treatment at 900 °C in argon [37]. v) Fluorination does not decrease drastically the specific surface area (loss of 40% in the worst case). A huge decomposition in F_2 gas is avoided by the use of mild conditions, i.e. both short duration and dilution of F_2 with an inert gas. vi) Micropores, which are hosting the most of the catalytic sites in Fe-based PEM fuel cell catalysts [76] are the more affected by fluorination. In order to keep the specific surface area and the pore volume as high as possible, porous carbonaceous must contain a small part of mesopores that are less sensitive to fluorination. As demonstrated in our recent works on non-Pt- [37], the present data will be useful for the design of porous N-doped carbon-based catalysts for the oxygen reduction in PEM fuel cells.

Acknowledgment

M.D. acknowledges I-Site CAP2025, Université Clermont Auvergne, and Clermont Auvergne Métropole for support via the Academie CAP20-25. S.R. INRS team acknowledges the support from the Natural Sciences and Engineering Research Council of Canada (NSERC).

References

[1] M. Inagaki, M. Toyoda, Y. Soneda, et T. Morishita, Nitrogen-doped carbon materials, *Carbon*, vol. 132, p. 104-140, 2018, doi: 10.1016/j.carbon.2018.02.024.

[2] H. Wang, M. Xie, L. Thia, A. Fisher, et X. Wang, Strategies on the Design of Nitrogen-Doped Graphene, *J. Phys. Chem. Lett.*, vol. 5, no 1, p. 119-125, 2014, doi: 10.1021/jz402416a.

[3] X. Wang, G. Sun, P. Routh, D.-H. Kim, W. Huang, et P. Chen, Heteroatom-doped graphene materials: syntheses, properties and applications, *Chem. Soc. Rev.*, vol. 43, no 20, p. 7067-7098, 2014, doi: 10.1039/C4CS00141A.

[4] H. Wang, T. Maiyalagan, et X. Wang, Review on Recent Progress in Nitrogen-Doped Graphene: Synthesis, Characterization, and Its Potential Applications, *ACS Catal.*, vol. 2, no 5, p. 781-794, 2012, doi: 10.1021/cs200652y.

[5] W. Yang and S. Chen, Biomass-Derived Carbon for Electrode Fabrication in Microbial Fuel Cells: A Review, *Ind. Eng. Chem. Res.*, vol. 59, no 14, p. 6391-6404, 2020, doi: 10.1021/acs.iecr.0c00041.

[6] L. Li, Y. Huang, et Y. Li, Carbonaceous materials for electrochemical CO2 reduction, *Energy Chem*, vol. 2, p. 23, 2020.

[7] L. Zhang, J. Xiao, H. Wang, et M. Shao, Carbon-Based Electrocatalysts for Hydrogen and Oxygen Evolution Reactions, *ACS Catal.*, vol. 7, no 11, p. 7855-7865, 2017.

[8] L. Dai, Y. Xue, L. Qu, H.-J. Choi, et J.-B. Baek, Metal-Free Catalysts for Oxygen Reduction Reaction, *Chem. Rev.*, vol. 115, no 11, p. 4823-4892, 2015, doi: 10.1021/cr5003563.

[9] K. Gong, F. Du, Z. Xia, M. Durstock, et L. Dai, Nitrogen-Doped Carbon Nanotube Arrays with High Electrocatalytic Activity for Oxygen Reduction, vol. 323, p. 5, 2009.

[10] J. Shui, M. Wang, F. Du, et L. Dai, N-doped carbon nanomaterials are durable catalysts for oxygen reduction reaction in acidic fuel cells, *Sci. Adv.*, vol. 1, no 1, 2015, doi: 10.1126/sciadv.1400129.

[11] H.-F. Wang, L. Chen, H. Pang, S. Kaskel, et Q. Xu, MOF-derived electrocatalysts for oxygen reduction, oxygen evolution and hydrogen evolution reactions, *Chem. Soc. Rev.*, vol. 49, no 5, p. 1414-1448, 2020, doi: 10.1039/C9CS00906J.

[12] W. Niu et Y. Yang, Graphitic Carbon Nitride for Electrochemical Energy Conversion and Storage, *ACS Energy Letters*, p. 20, 2018.

[13] J. Duan, S. Chen, M. Jaroniec, et S. Z. Qiao, Heteroatom-Doped Graphene-Based Materials for Energy-Relevant Electrocatalytic Processes, *ACS Catal.*, vol. 5, no 9, p. 5207-5234, 2015, doi: 10.1021/acscatal.5b00991.

[14] D. Qiu, A. Gao, Z. Xie, L. Zheng, C. Kang, Y. Li, *et al.*, Homologous Hierarchical Porous Hollow Carbon Spheres Anode and Bowls Cathode Enabling High-Energy Sodium-Ion Hybrid Capacitors, *ACS Appl. Mater. Interfaces*, vol. 10, p. 44483-44493, 2018.
[15] J. Jiang, P. Nie, B. Ding, Y. Zhang, G. Xu, L. Wu *et al.*, Highly stable lithium ion capacitor enabled by hierarchical polyimide derived carbon microspheres combined with 3D current collectors, *J. Mater. Chem. A*, vol. 5, no 44, p. 23283-23291, 2017, doi: 10.1039/C7TA05972H.
[16] K. Zou, P. Cai, X. Cao, G. Zou, H. Hou, et X. Ji, Carbon materials for high-performance lithium-ion capacitor, *Current Opinion in Electrochemistry*, vol. 21, p. 31-39, 2020, doi: 10.1016/j.coelec.2020.01.005.
[17] A. Shah, A. Zahid, H. Subhan, A. Munir, F. J. Iftikhar, et M. Akbar, Heteroatom-doped carbonaceous electrode materials for high performance energy storage devices, *Sustainable Energy Fuels*, vol. 2, no 7, p. 1398-1429, 2018, doi: 10.1039/C7SE00548B.
[18] G. Zhou, Long-life Li/polysulphide batteries with high sulphur loading enabled by lightweight three-dimensional nitrogen/sulphur-codoped graphene sponge, *NATURE COMMUNICATIONS*, p. 11, 2015.
[19] L.-C. Yin, J. Liang, G.-M. Zhou, F. Li, R. Saito, et H.-M. Cheng, Understanding the interactions between lithium polysulfides and N-doped graphene using density functional theory calculations, *Nano Energy*, vol. 25, p. 203-210, 2016, doi: 10.1016/j.nanoen.2016.04.053.
[20] S. Niu, W. Lv, G. Zhou, H. Shi, X. Qin, C. Zheng *et al.*, Electrostatic-spraying an ultrathin, multifunctional and compact coating onto a cathode for a long-life and high-rate lithium-sulfur battery, *Nano Energy*, vol. 30, p. 138-145, 2016, doi: 10.1016/j.nanoen.2016.09.044.
[21 K. Han, J. Shen, S. Hao, H. Ye, C. Wolverton, M. C. Kung *et al.*, Free-Standing Nitrogen-doped Graphene Paper as Electrodes for High-Performance Lithium/Dissolved Polysulfide Batteries, *Chem. Sus. Chem.*, vol. 7, p. 2545-2477, 2014.
[22] H. M. Jeong, J. W. Lee, W. H. Shin, Y. J. Choi, H. J. Shin, J. K. Kang *et al.*, Nitrogen-Doped Graphene for High-Performance Ultracapacitors and the Importance of Nitrogen-Doped Sites at Basal Planes, *Nano Lett.*, vol. 11, no 6, p. 2472-2477, 2011, doi: 10.1021/nl2009058.
[23] J. Ding, W. Hu, E. Paek, et D. Mitlin, Review of Hybrid Ion Capacitors: From Aqueous to Lithium to Sodium, *Chem. Rev.*, vol. 118, no 14, p. 6457-6498, 2018, doi: 10.1021/acs.chemrev.8b00116.
[24] R. Li, J. Huang, J. Li, L. Cao, X. Zhong, A. Yu *et al.*, Nitrogen-doped porous hard carbons derived from shaddock peel for high-capacity lithium-ion battery anodes, *Journal of Electroanalytical Chemistry*, vol. 862, p. 114044, 2020, doi: 10.1016/j.jelechem.2020.114044.
[25] J. Li, K. Han, D. Wang, Z. Teng, Y. Cao, J. Qi *et al.*, Fabrication of high performance structural N-doped hierarchical porous carbon for supercapacitors, *Carbon*, vol. 164, p. 42-50, 2020, doi: 10.1016/j.carbon.2020.03.044.
[26] M. Nakayama, K. Komine, et D. Inohara, Nitrogen-Doped Carbon Cloth for Supercapacitors Prepared via a Hydrothermal Process, *J. Electrochem. Soc.*, vol. 163, no 10, p. A2428-A2434, 2016, doi: 10.1149/2.0091613jes.
[27] C. L. Mangun, K. R. Benak, J. Economy, et K. L. Foster, Surface chemistry, pore sizes and adsorption properties of activated carbon fibers and precursors treated with ammonia, *Carbon*, vol. 39, no 12, p. 1809-1820, 2001, doi: 10.1016/S0008-6223(00)00319-5.
[28] G. Zuo, A. Xie, J. Li, T. Su, X. Pan, et W. Dong, Large Emission Red-Shift of Carbon Dots by Fluorine Doping and Their Applications for Red Cell Imaging and Sensitive Intracellular Ag + Detection, *J. Phys. Chem. C*, vol. 121, no 47, p. 26558-26565, 2017, doi: 10.1021/acs.jpcc.7b10179.
[29] J. Wang, X. Hu, H. Ding, X. Huang, M. Xu, Z. Li *et al.*, Fluorine and Nitrogen Co-Doped Carbon Dot Complexation with Fe(III) as a *T* 1 Contrast Agent for Magnetic Resonance Imaging, *ACS Appl. Mater. Interfaces*, vol. 11, no 20, p. 18203-18212, 2019, doi: 10.1021/acsami.9b03644.
[30] S. Akula, B. Balasubramaniam, P. Varathan, et A. K. Sahu, Nitrogen–Fluorine Dual Doped Porous Carbon Derived from Silk Cotton as Efficient Oxygen Reduction Catalyst for Polymer Electrolyte Fuel Cells, *ACS Appl. Energy Mater.*, vol. 2, no 5, p. 3253-3263, 2019, doi: 10.1021/acsaem.9b00100.

[31] P. Zhu, J. Gao, X. Chen, et S. Liu, An efficient metal-free bifunctional oxygen electrocatalyst of carbon co-doped with fluorine and nitrogen atoms for rechargeable Zn-air battery, *International Journal of Hydrogen Energy*, vol. 45, no 16, p. 9512-9521, 2020, doi: 10.1016/j.ijhydene.2020.01.131.
[32] Y. Sim, S. J. Kim, G. Janani, Y. Chae, S. Surendran, H. Kim *et al.*, The synergistic effect of nitrogen and fluorine co-doping in graphene quantum dot catalysts for full water splitting and supercapacitor, *Applied Surface Science*, vol. 507, p. 145157, 2020, doi: 10.1016/j.apsusc.2019.145157.
[33] Y. Ligay. F. Musico, N. Kakati, M. F. M. Labata, J. D. Ocon, et P.-Y. A. Chuang, One-pot hydrothermal synthesis of heteroatom co-doped with fluorine on reduced graphene oxide for enhanced ORR activity and stability in alkaline media, *Materials Chemistry and Physics*, vol. 236, p. 121804, 2019, doi: 10.1016/j.matchemphys.2019.121804.
[34] Q. He, J. Jiang, J. Zhu, Z. Pan, C. Li, M. Yu et al., A facile and cost effective synthesis of nitrogen and fluorine Co-doped porous carbon for high performance Sodium ion battery anode material, *Journal of Power Sources*, vol. 448, p. 227568, 2020, doi: 10.1016/j.jpowsour.2019.227568.
[35] S. Berthon-Fabry, L. Dubau, Y. Ahmad, K. Guerin, et M. Chatenet, First Insight into Fluorinated Pt/Carbon Aerogels as More Corrosion-Resistant Electrocatalysts for Proton Exchange Membrane Fuel Cell Cathodes, *Electrocatalysis*, vol. 6, no 6, p. 521-533, 2015, doi: 10.1007/s12678-015-0267-9.
[36] T. Asset, R. Chattot, F. Maillard, L. Dubau, Y. Ahmad, N. Batisse et al., Activity and Durability of Platinum-Based Electrocatalysts Supported on Bare or Fluorinated Nanostructured Carbon Substrates, *J. Electrochem. Soc.*, vol. 165, no 6, p. F3346-F3358, 2018, doi: 10.1149/2.031806jes.
[37] G. Zhang, X. Yang, M. Dubois, M. Herraiz, R. Chenitz, M. Lefèvre *et al.*, Non-PGM electrocatalysts for PEM fuel cells: effect of fluorination on the activity and stability of a highly active NC_Ar + NH3 catalyst, *Energy Environ. Sci.*, vol. 12, no 10, p. 3015-3037, 2019, doi: 10.1039/C9EE00867E.
[38] A. S. Arico, V. Antonucci, M. Minutoli, et N. Giordano, The influence of functional groups on the surface acid-base characteristics of carbon blacks, *Carbon*, vol. 27, no 3, p. 337-347, 1989, doi: 10.1016/0008-6223(89)90065-1.
[39] M. L. González-Martín, B. Jańczuk, L. Labajos-Broncano, et J. M. Bruque, Determination of the Carbon Black Surface Free Energy Components from the Heat of Immersion Measurements, *Langmuir*, vol. 13, no 22, p. 5991-5994, 1997, doi: 10.1021/la9621224.
[40] H. Meng, F. Jaouen, E. Proietti, M. Lefèvre, et J.-P. Dodelet, pH-effect on oxygen reduction activity of Fe-based electro-catalysts, *Electrochemistry Communications*, vol. 11, no 10, p. 1986-1989, 2009, doi: 10.1016/j.elecom.2009.08.035.
[41] G. Zhang, R. Chenitz, M. Lefèvre, S. Sun, et J.-P. Dodelet, Is iron involved in the lack of stability of Fe/N/C electrocatalysts used to reduce oxygen at the cathode of PEM fuel cells?, *Nano Energy*, vol. 29, p. 111-125, 2016, doi: 10.1016/j.nanoen.2016.02.038.
[42] E. Proietti, F. Jaouen, M. Lefèvre, N. Larouche, J. Tian, J. Herranz et al., Iron-based cathode catalyst with enhanced power density in polymer electrolyte membrane fuel cells, *Nat Commun*, vol. 2, no 1, p. 416, 2011, doi: 10.1038/ncomms1427.
[43] F. Chamssedine, M. Dubois, K. Guérin, J. Giraudet, F. Masin, D. Ivano, Reactivity of Carbon Nanofibers with Fluorine Gas, *Chem. Mater.*, vol. 19, no 2, p. 161-172, 2007, doi: 10.1021/cm061731m.
[44] A. P. Kharitonov, Direct fluorination of polymers—From fundamental research to industrial applications, *Progress in Organic Coatings*, vol. 61, no 2-4, p. 192-204, 2008, doi: 10.1016/j.porgcoat.2007.09.027.
[45] J. Peyroux, M. Dubois, E.Tomasella, N. Batisse, P. Thomas, Surface modification of low-density polyethylene packaging film via direct fluorination, *Surface and Coatings Technology*, vol. 292, p. 144-154, 2016, doi: 10.1016/j.surfcoat.2016.03.021.
[46] C. Matei Ghimbeu, K. Guerin, M. Dubois, S. Hajjar-Garreau, C. Vix-Guterl, Insights on the reactivity of ordered porous carbons exposed to different fluorinating agents and conditions, *Carbon*, vol. 84, p. 567-583, 2015, doi: 10.1016/j.carbon.2014.12.034.

[47] J. Parmentier, S. Schlienger, M. Dubois, E. Disa, F. Masin, T. A. Centeno, Structural/textural properties and water reactivity of fluorinated activated carbons, *Carbon*, vol. 50, no 14, p. 5135-5147, 2012, doi: 10.1016/j.carbon.2012.06.054.
[48] H. Touhara, F. Okino, Property control of carbon materials by fluorination, *Carbon*, vol. 38, p. 241-267, 2000.
[49] N. Watanabe, Two types of graphite fluorides, (CF)n and (C2F)n, and discharge characteristics and mechanisms of electrodes of (CF)n and (C2F)n in lithium batteries, *Solid State Ionics*, vol. 1, no 1-2, p. 87-110, 1980, doi: 10.1016/0167-2738(80)90025-9.
[50] M. Dubois, K. Guérin, J. P. Pinheiro, Z. Fawal, F. Masin, A. Hamwi, NMR and EPR studies of room temperature highly fluorinated graphite heat-treated under fluorine atmosphere, *Carbon*, vol. 42, no 10, Art. no 10, 2004, doi: 10.1016/j.carbon.2004.03.025.
[51] J. Giraudet, M. Dubois, K. Guérin, C. Delabarre, A. Hamwi, F. Masin, Solid-State NMR Study of the Post-Fluorination of (C 2.5 F) *n* Fluorine−GIC, *J. Phys. Chem. B*, vol. 111, no 51, p. 14143-14151, 2007, doi: 10.1021/jp076170g.
[52] K. Guérin, J. P. Pinheiro, M. Dubois, Z. Fawal, F. Masin, R. Yazami *et al.*, Synthesis and Characterization of Highly Fluorinated Graphite Containing sp 2 and sp 3 Carbon, *Chem. Mater.*, vol. 16, no 9, p. 1786-1792, 2004, doi: 10.1021/cm034974c.
[53] Y. Sato, K. Itoh, R. Hagiwara, T. Fukunaga, Y. Ito, On the so-called « semi-ionic » C–F bond character in fluorine–GIC, *Carbon*, vol. 42, no 15, p. 3243-3249, 2004, doi: 10.1016/j.carbon.2004.08.012.
[54] M. Mar, M. Dubois, K. Guérin, N. Batisse, B. Simon, et P. Bernard, Tuning fluorine and oxygen distribution in graphite oxifluorides for enhanced performances in primary lithium battery, *Carbon*, vol. 141, p. 6-15, 2019, doi: 10.1016/j.carbon.2018.09.037.
[55] C. Y. Liang et S. Krimm, Infrared Spectra of High Polymers. III. Polytetrafluoroethylene and Polychlorotrifluoroethylene, *The Journal of Chemical Physics*, vol. 25, no 3, p. 563-571, 1956, doi: 10.1063/1.1742964.
[56] J. I. Robson, L. K. Gohar, M. D. Hurley, K. P. Shine, et T. J. Wallington, Revised IR spectrum, radiative efficiency and global warming potential of nitrogen trifluoride, *Geophys. Res. Lett.*, vol. 33, no 10, 2006, doi: 10.1029/2006GL026210.
[57] A. M. Panich, Nuclear magnetic resonance study of fluorine–graphite intercalation compounds and graphite fluorides, *Synthetic Metals*, vol. 100, no 2, Art. no 2, 1999, doi: 10.1016/S0379-6779(98)01512-4.
[58] J. Giraudet, M. Dubois, A. Hamwi, W. E. E. Stone, P. Pirotte, F. Masin, Solid-State NMR 19F and 13C Study of Graphite Monofluoride (CF)n : 19 F Spin−Lattice Magnetic Relaxation and 19F 13 C Distance Determination by Hartmann−Hahn Cross Polarization, *J. Phys. Chem. B*, vol. 109, no 1, p. 175-181, 2005, doi: 10.1021/jp046833j.
[59] T. Mallouk, B. Hawkins, M. Conrad, K. Zilm, G. Maciel, N. Bartlett, Raman, infrared and n.m.r. studies of the graphite hydrofluorides C x F 1-δ (HF) δ (2 ≤ x ≤ 5), *Phil. Trans. R. Soc. Lond. A*, vol. 314, no 1528, p. 179-187, 1985, doi: 10.1098/rsta.1985.0017.
[60] W. Zhang, M. Dubois, K. Guérin, P. Bonnet, H. Kharbache, F. Masin, et al., Effect of curvature on C–F bonding in fluorinated carbons: from fullerene and derivatives to graphite, *Phys. Chem. Chem. Phys.*, vol. 12, no 6, Art. no 6, 2010.
[61] M. Dubois, J. Giraudet, K. Guérin, A. Hamwi, Z. Fawal, P. Pirotte, EPR and Solid-State NMR Studies of Poly(dicarbon monofluoride) (C2F)n, *J. Phys. Chem. B*, vol. 110, no 24, p. 11800-11808, 2006, doi: 10.1021/jp061291m.
[62] W. Zhang, P. Bonnet, M. Dubois, C. Ewels, K. Guerin, et E. Petit, Comparative study of SWCNT fluorination by atomic and molecular fluorine, *Chem. Mater.*, no 24, p. 1744-51, 2012.
[63] F. Leroux, M. Dubois, Origin of the highly enhanced porosity of styryl LDH hybrid-type carbon replicas and study of a subsequent fluorination at low-temperature, *J. Mater. Chem.*, vol. 16, no 46, p. 4510, 2006, doi: 10.1039/b610058a.

[64] X. Wang, Y. Chen, Y. Dai, Q. Wang, J. Gao, J. Huang, et al., Preparing Highly Fluorinated Multiwall Carbon Nanotube by Direct Heating-Fluorination during the Elimination of Oxygen-Related Groups, *J. Phys. Chem. C*, vol. 117, no 23, p. 12078-12085, 2013, doi: 10.1021/jp312801p.
[65] M. Dubois, K. Guérin, Y. Ahmad, N. Batisse, M. Mar, L. Frezet, et al. Thermal exfoliation of fluorinated graphite, *Carbon*, vol. 77, p. 688-704, 2014, doi: 10.1016/j.carbon.2014.05.074.
[66] Y. Sato, K. Itoh, R. Hagiwara, T. Fukunaga, Y. Ito, Short-range structures of poly(dicarbon monofluoride) (C2F)n and poly(carbon monofluoride) (CF)n, *Carbon*, vol. 42, no 14, p. 2897-2903, 2004, doi: 10.1016/j.carbon.2004.06.042.
[67] S. Kwon, J.-H. Ko, K.-J. Jeon, Y.-H. Kim, et J. Y. Park, Enhanced Nanoscale Friction on Fluorinated Graphene, *Nano Lett.*, vol. 12, no 12, p. 6043-6048, 2012, doi: 10.1021/nl204019k.
[68] J. T. Robinson, J. S. Burgess, C. E. Junkermeier, S. C. Badescu, T. L. Reinecke, F. Keith Perkins *et al.*, Properties of Fluorinated Graphene Films, *Nano Lett.*, vol. 10, no 8, p. 3001-3005, 2010, doi: 10.1021/nl101437p.
[69] T. V. Reshetenko, J. St-Pierre, K. P. Bethune, K. Artyushkova, R. Rocheleau, et P. Atanassov, Multi-Analytical Study of Gas Diffusion Layer PTFE Content Local Variation, *ECS Transactions*, vol. 50, no 2, p. 591-599, 2013, doi: 10.1149/05002.0591ecst.
[70] R. Thorpe, S. Rangan, R. Whitcomb, A. C. Basaran, T. Saerbeck, I. K. Schuller *et al.*, The solid state conversion reaction of epitaxial FeF2 (110) thin films with lithium studied by angle-resolved X-ray photoelectron spectroscopy, *Phys. Chem. Chem. Phys.*, vol. 17, no 23, p. 15218-15225, 2015, doi: 10.1039/C5CP01150G.
[71] J. H. Sanders, J. N. Cutler, et G. John, Characterization of surface layers on M-50 steel exposed to perfluoropolyalkyethers at elevated temperatures, *Applied Surface Science*, vol. 135, no 1-4, p. 169-177, 1998, doi: 10.1016/S0169-4332(98)00273-6.
[72] G. Zhang, S. Sun, D. Yang, J.-P. Dodelet, E. Sacher, The surface analytical characterization of carbon fibers functionalized by H2SO4/HNO3 treatment, *Carbon*, vol. 46, no 2, p. 196-205, 2008, doi: 10.1016/j.carbon.2007.11.002.
[73] G. Zhang, D. Yang, E. Sacher, Structure and Morphology of Co Nanoparticles Deposited onto Highly Oriented Pyrolytic Graphite, *J. Phys. Chem. C*, vol. 111, no 46, p. 17200-17205, 2007, doi: 10.1021/jp074762t.
[74] I. Matanovic, K. Artyushkova, P. Atanassov, Understanding PGM-free catalysts by linking density functional theory calculations and structural analysis: Perspectives and challenges, *Current Opinion in Electrochemistry*, vol. 9, p. 137-144, 2018, doi: 10.1016/j.coelec.2018.03.009.
[75] X. Y. Fan, Z. J. Li, A. L. Meng, C. Li, Z. G. Wu, P. X. Yan, Study on the structure, morphology and properties of Fe-doped Cu 3 N films, *J. Phys. D: Appl. Phys.*, vol. 47, no 18, p. 185304, 2014, doi: 10.1088/0022-3727/47/18/185304.
[76] F. Jaouen, M. Lefèvre, J. P. Dodelet, M. Cai, Heat-treated Fe/N/C catalysts for O2 electroreduction: Are active sites located in micropores?, *J. Phys. Chem. B*, vol. 110, n°11, p. 5553-5558, 2006, doi:10.1021/jp057135h

Figures and tables

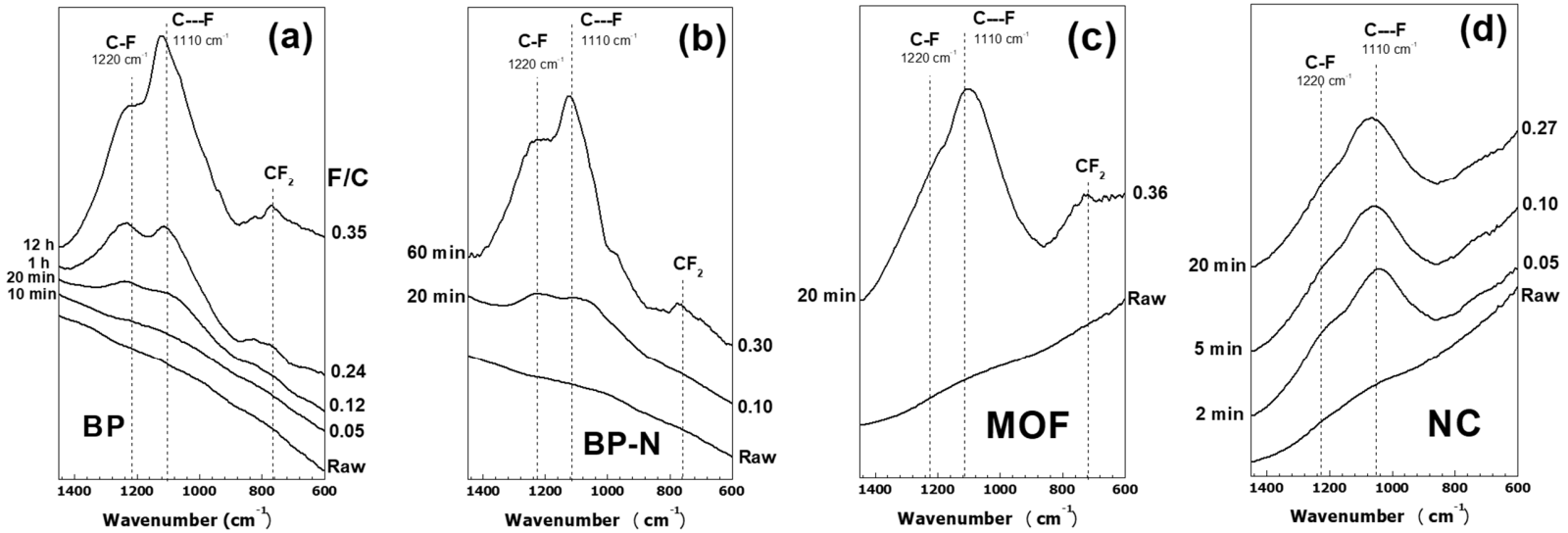

Figure 1: FTIR (Attenuated Total Reflectance [ATR]) spectra of raw and fluorinated samples, i.e, the four series: BP, BP-N, MOF, and NC.

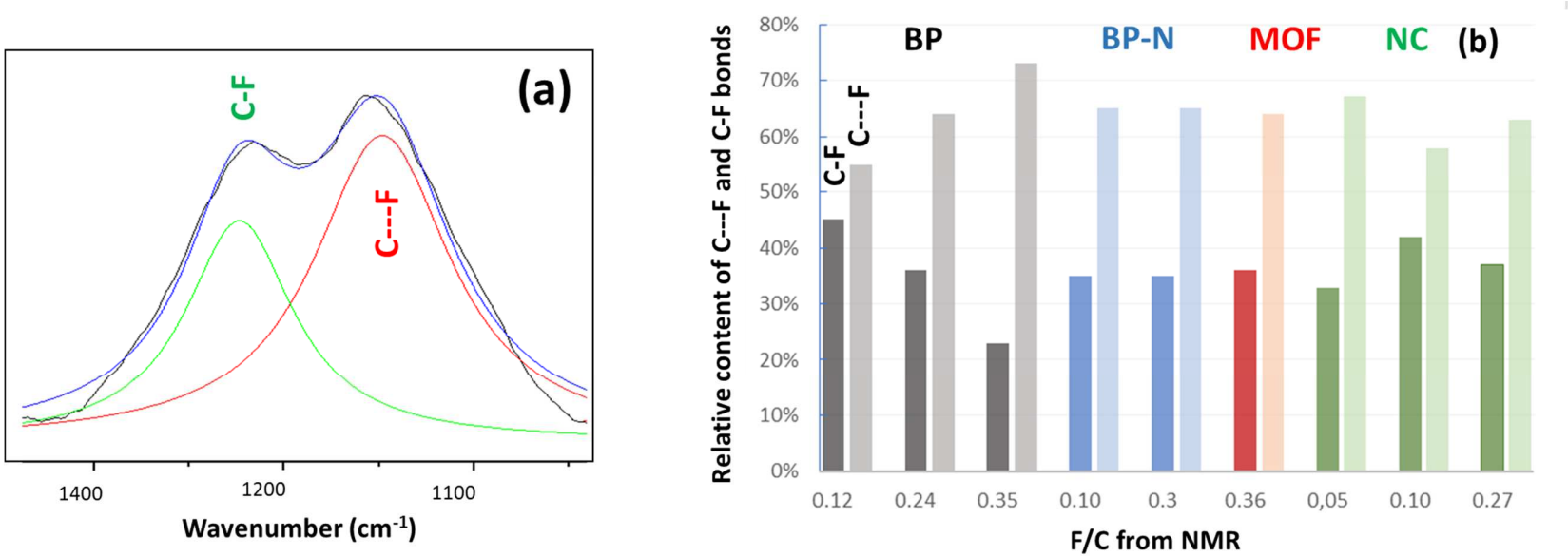

Figure 2: (a) Representative example of deconvolution of FTIR spectrum in the 850-1450 cm^{-1} range (F60min-BP). (b) Relative contents of two types of C-F bonds from FTIR.

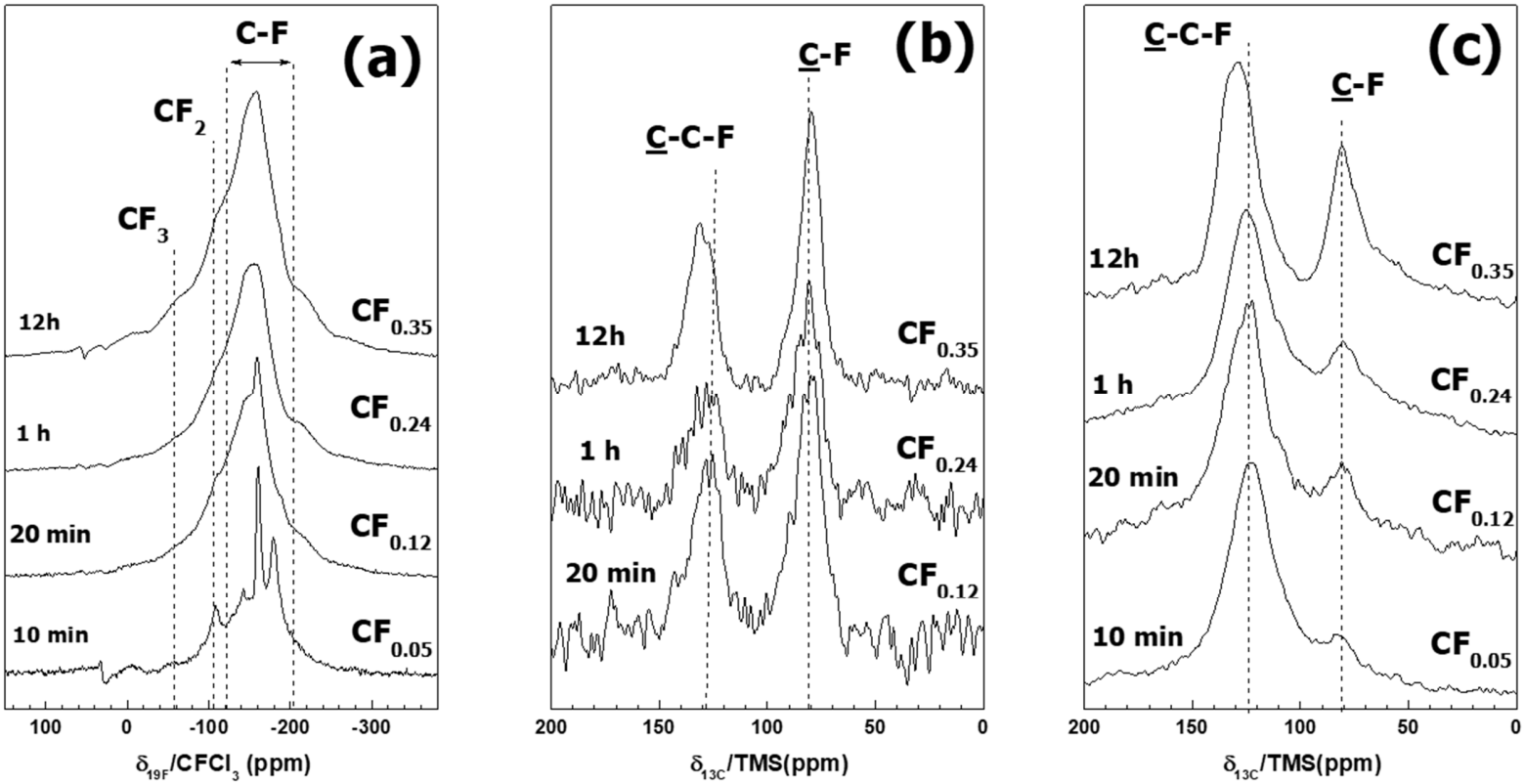

Figure 3: Spectra of fluorinated BP, (a) ^{19}F Magic Angle Spinning [MAS], 14 kHz NMR spectra of F10min-BP, F20min-BP, F1h-BP, and F12h-BP, (b) $^{19}F \rightarrow {}^{13}C$ Cross Polarization [CP] NMR spectra and ^{13}C MAS 10 kHz NMR spectra (c) of the same samples.

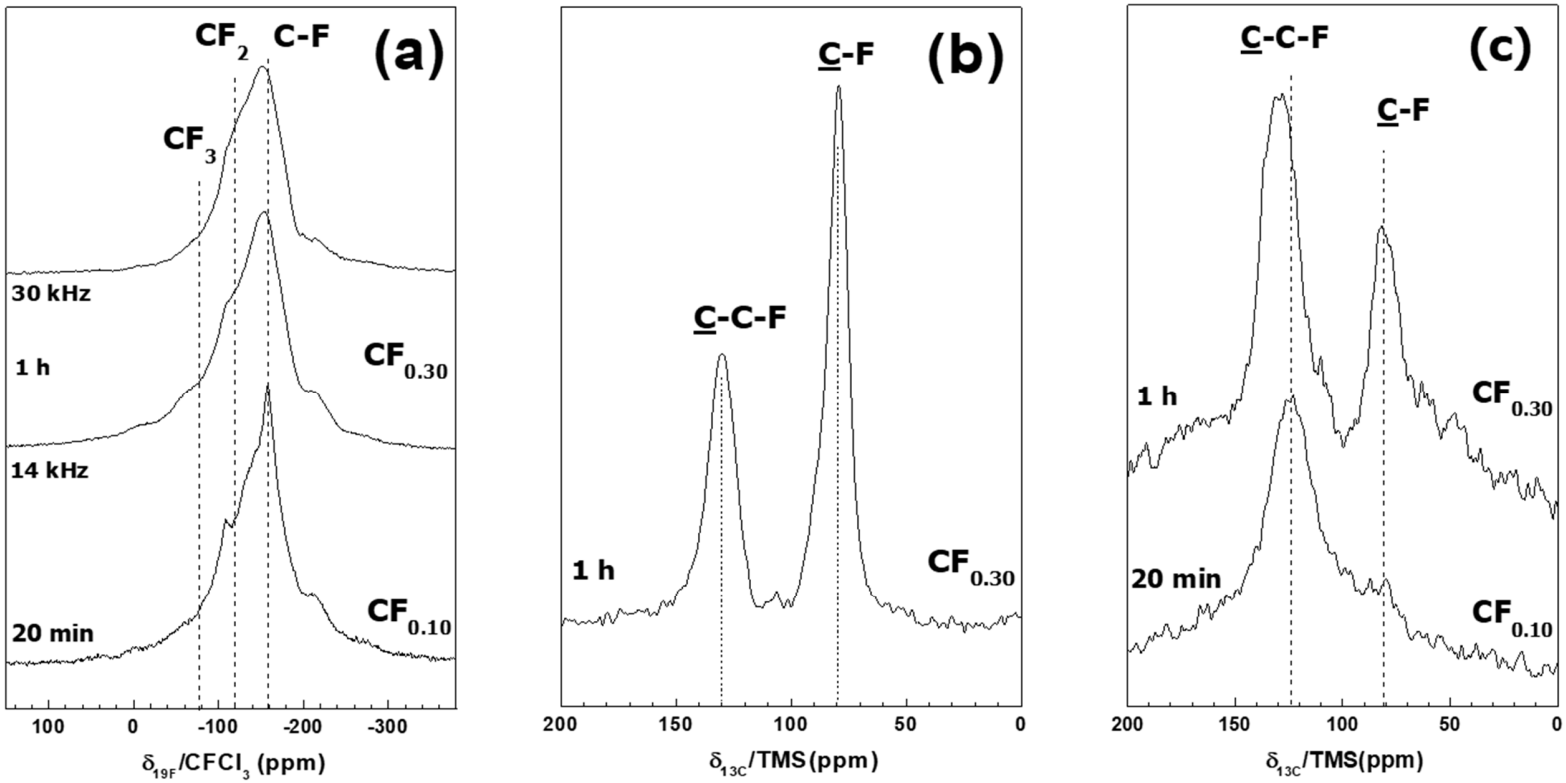

Figure 4: Spectra of fluorinated BP-N, (a) ^{19}FMagic Angle Spinning [MAS] 14 kHz NMR spectra of F20min-BP-N, F60min-BP-N, (b) $^{19}F \rightarrow {}^{13}C$ Cross Polarization [CP] NMR spectra of the same samples, ^{13}C MAS 10 kHz NMR spectra of the same samples.

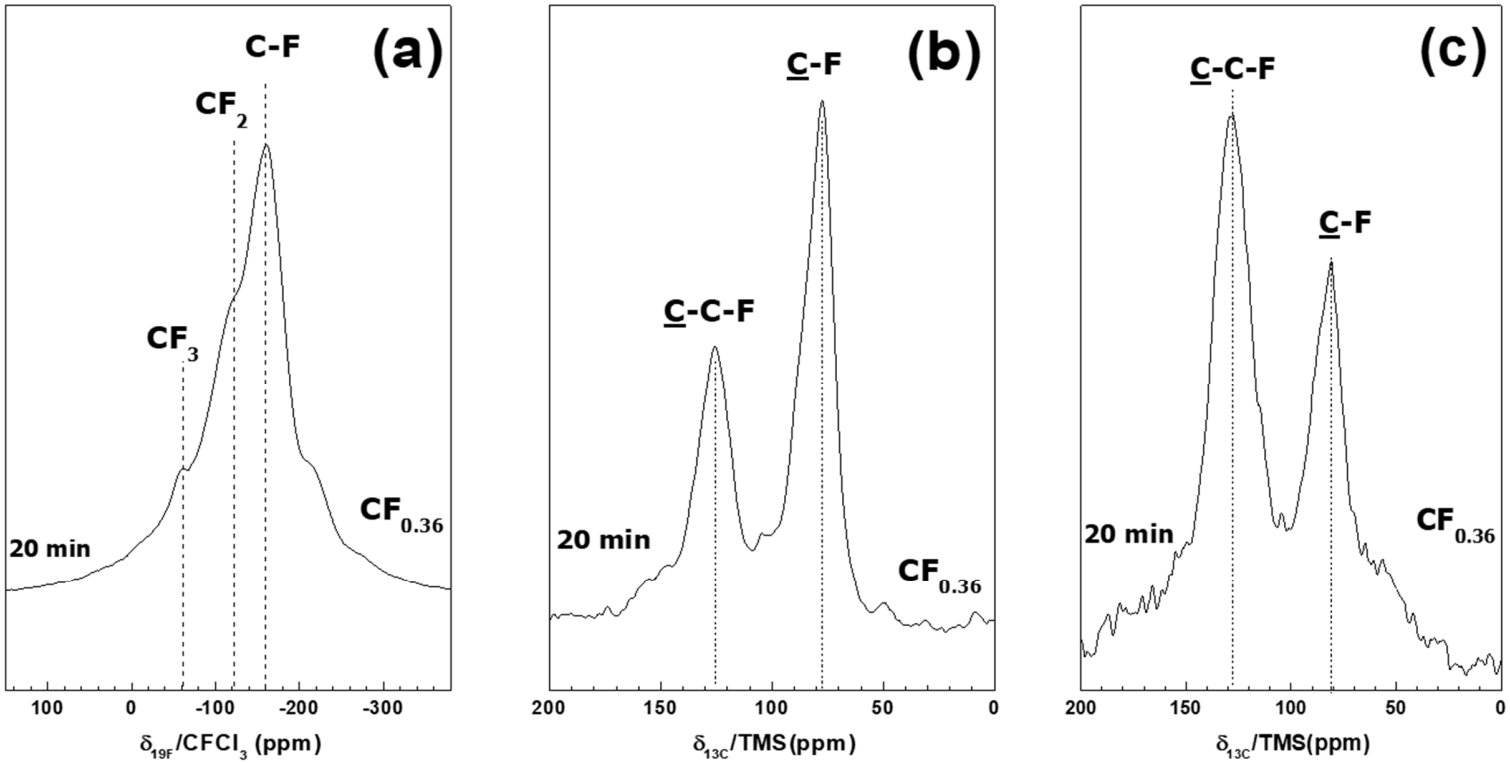

Figure 5: Spectra of fluorinated MOF, (a) ^{19}FMagic Angle Spinning [MAS] 14 kHz NMR spectrum, (b) ^{19}F→^{13}C Cross Polarization [CP] NMR spectrum and ^{13}C MAS 10 kHz NMR spectrum (c).

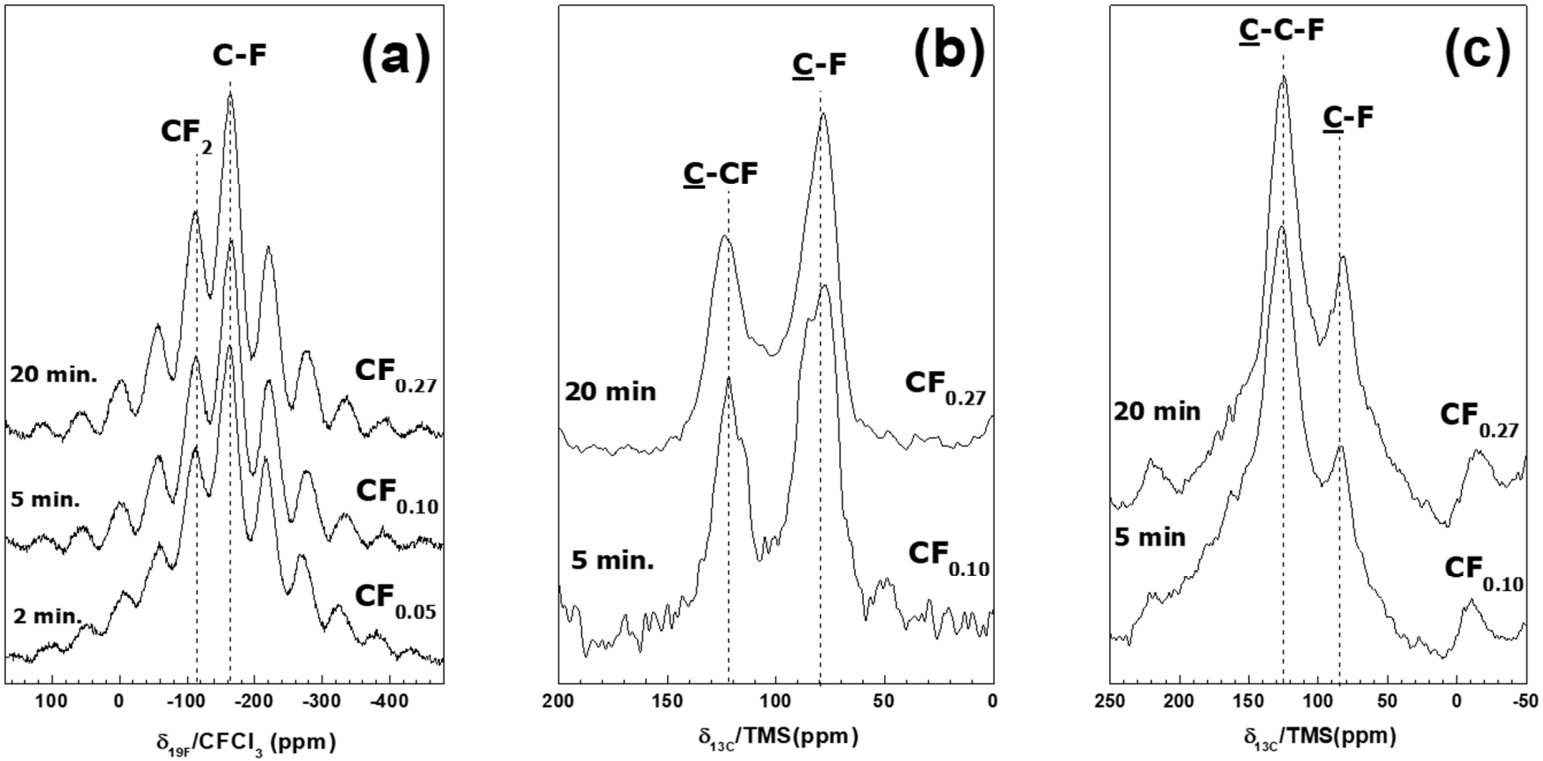

Figure 6: Spectra of fluorinated NC, (a) ^{19}F Magic Angle Spinning [MAS], 14 kHz NMR spectra of F2min-NC, F5min-NC, F1h-BP, and F20min-NC, (b) $^{19}F \rightarrow {}^{13}C$ Cross Polarization [CP] NMR spectra and (c) ^{13}C MAS 10 kHz NMR spectra of the same samples.

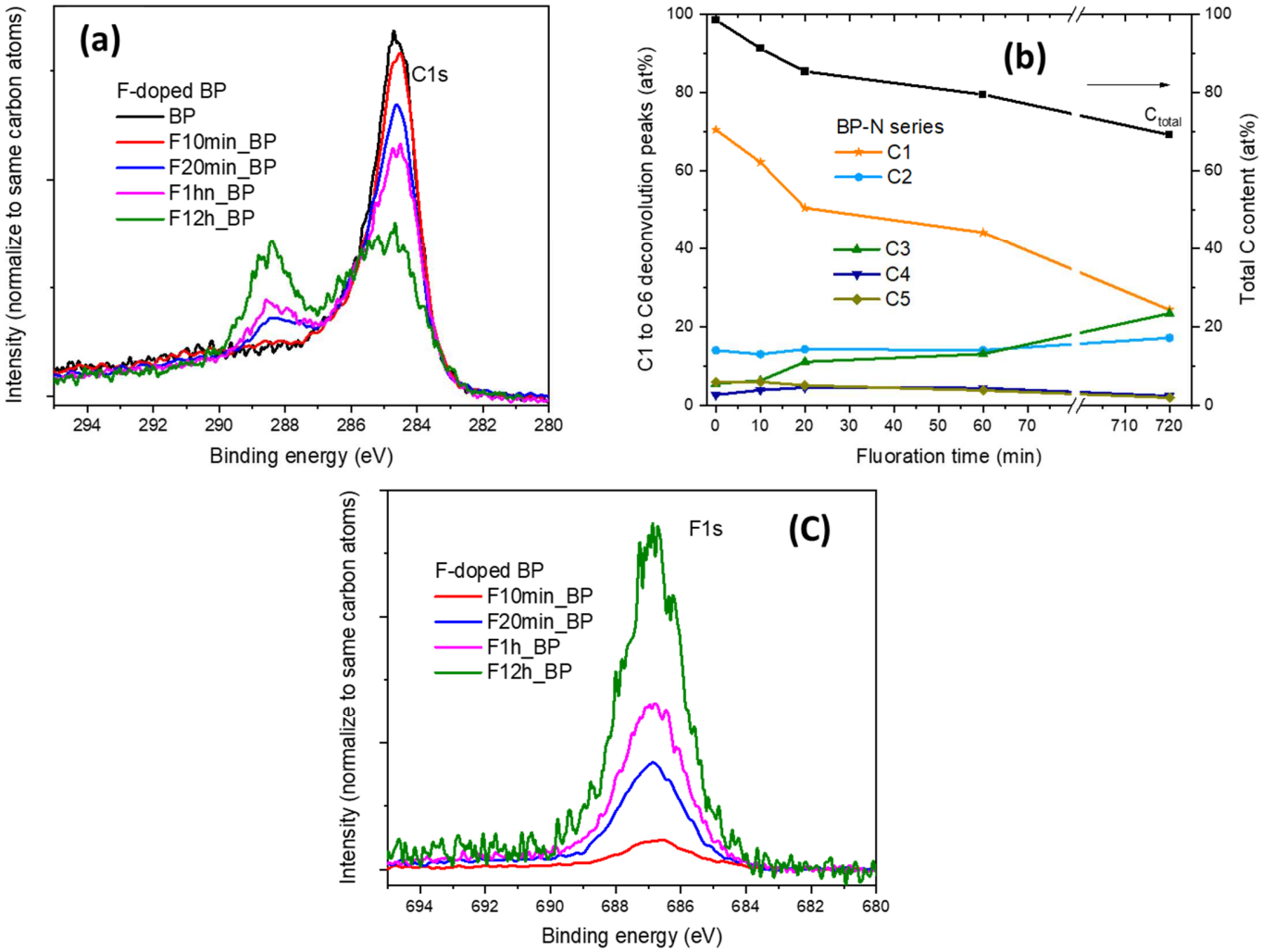

Figure 7: Change in the C1s (a, b) F1s (c) XPS spectra for BP series.

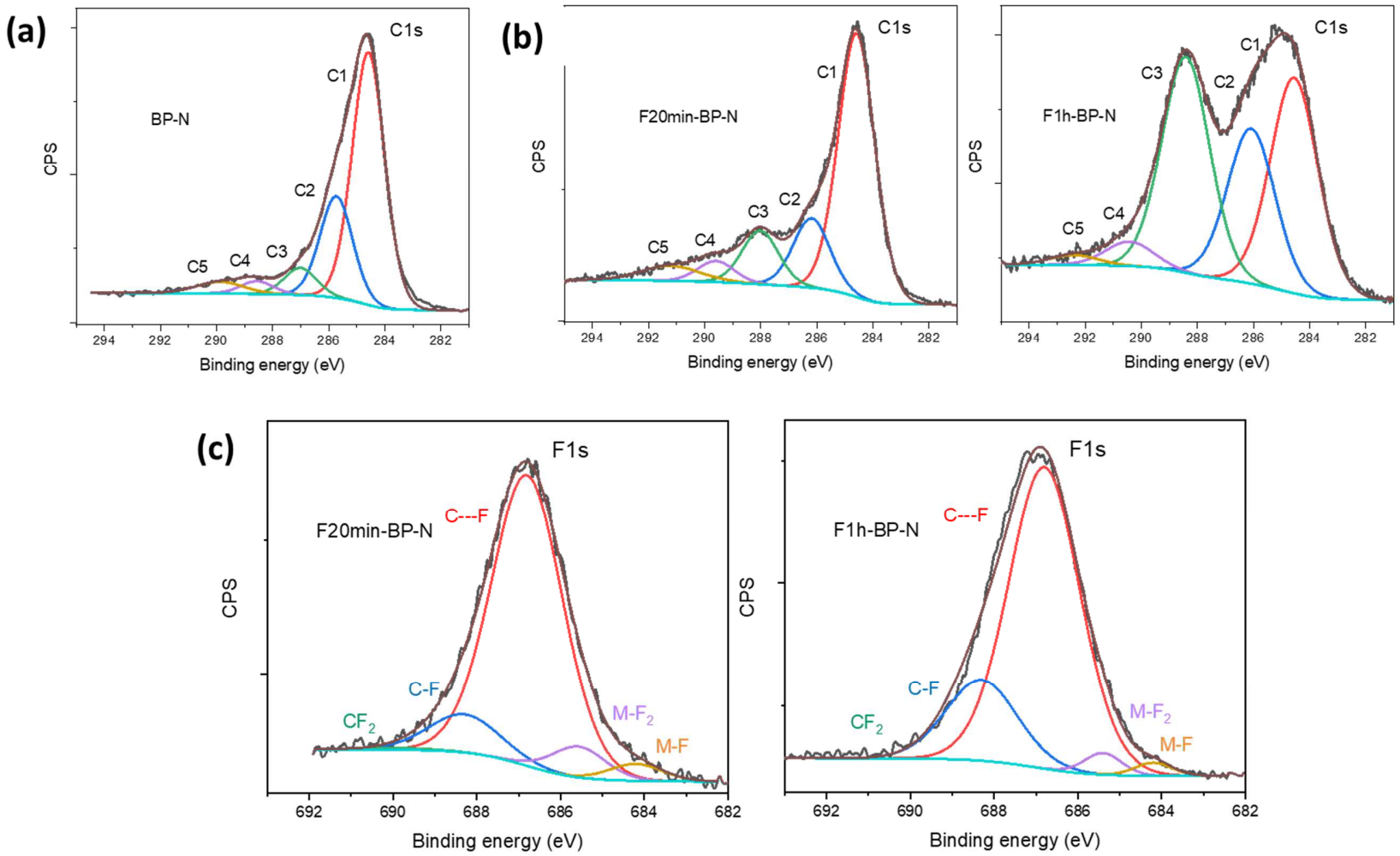

Figure 8: Change in the C1s (a, b) F1s (c) XPS spectra for BP-N series.

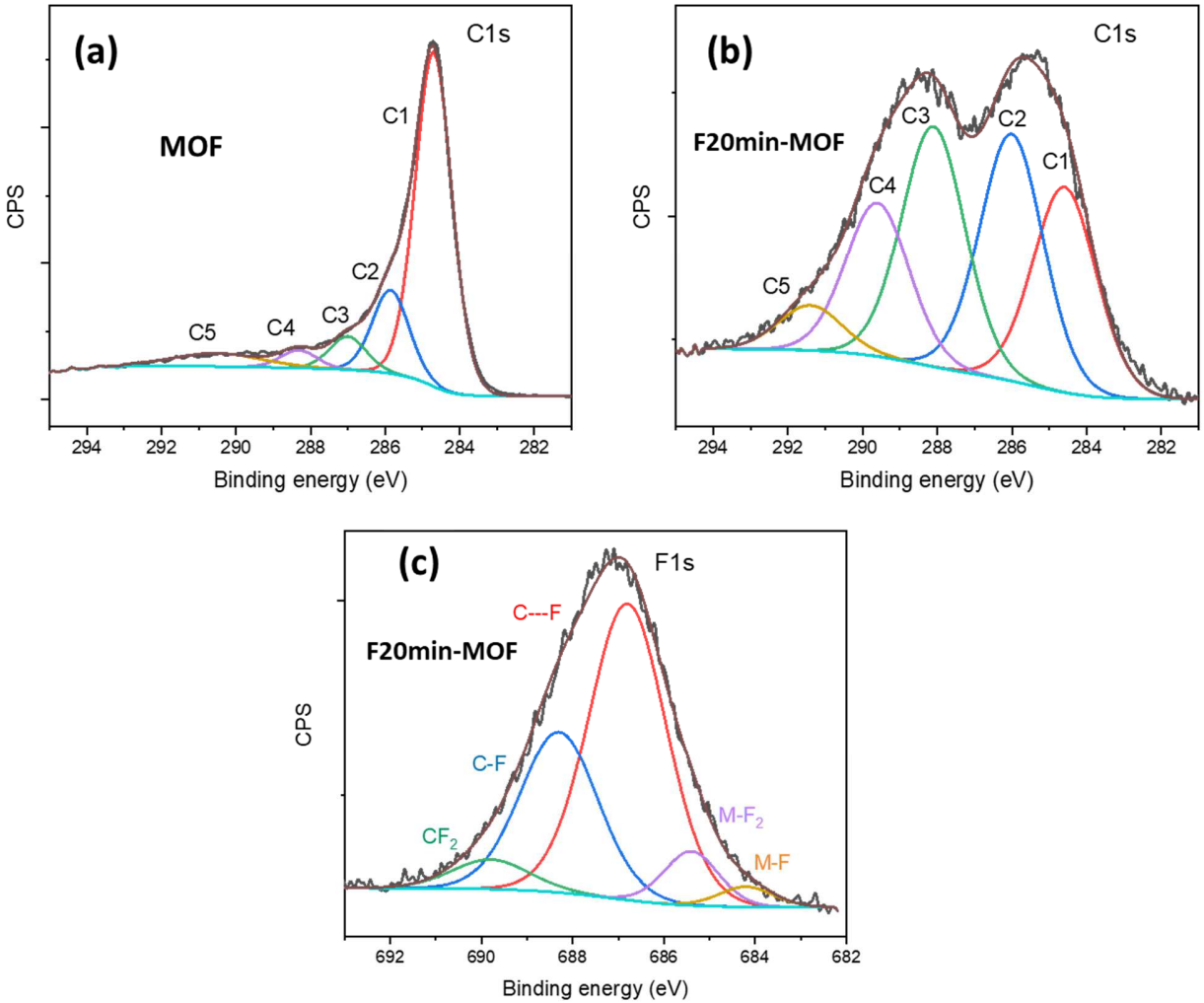

Figure 9: Deconvolution of the C1s (a,b) and F1s (c) XPS spectra for MOF series.

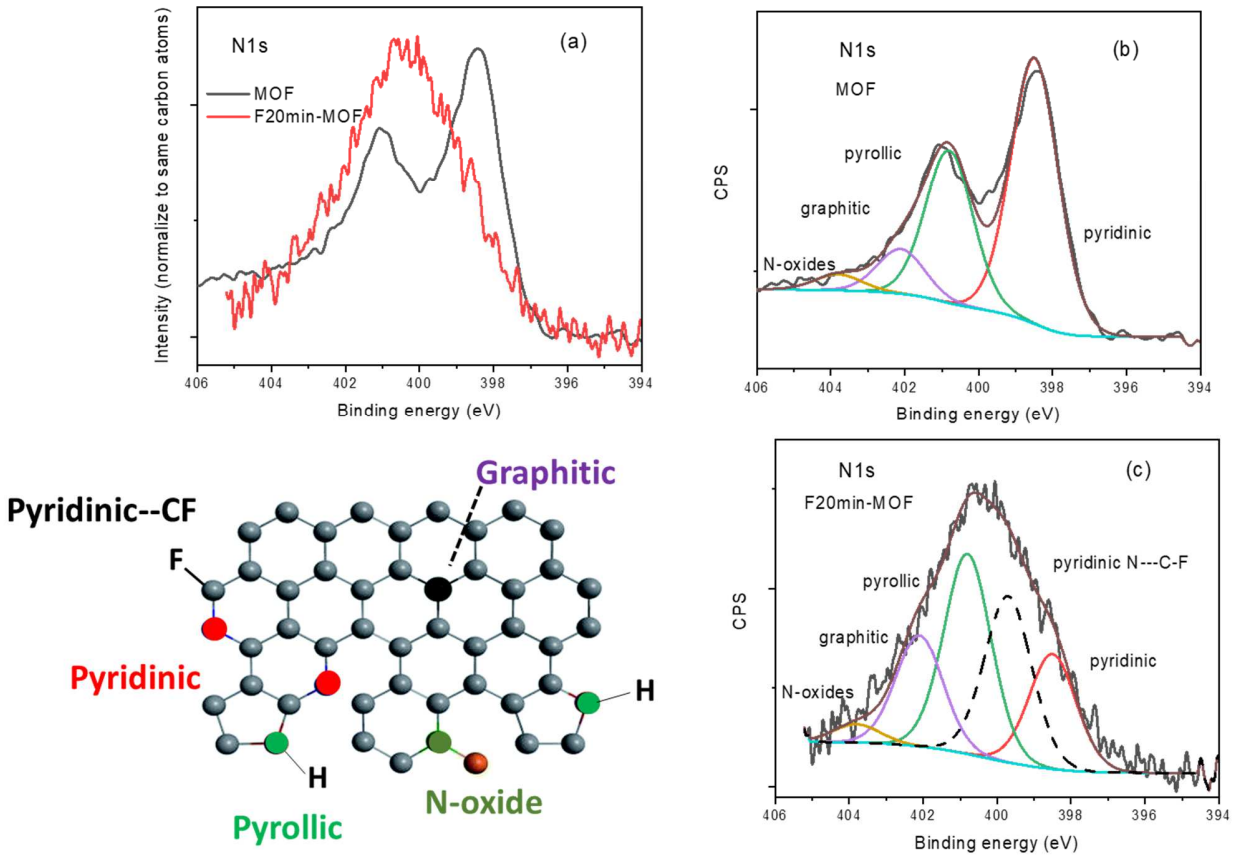

Figure 10: Deconvolution of the N1s XPS spectra for raw and fluorinated MOF.

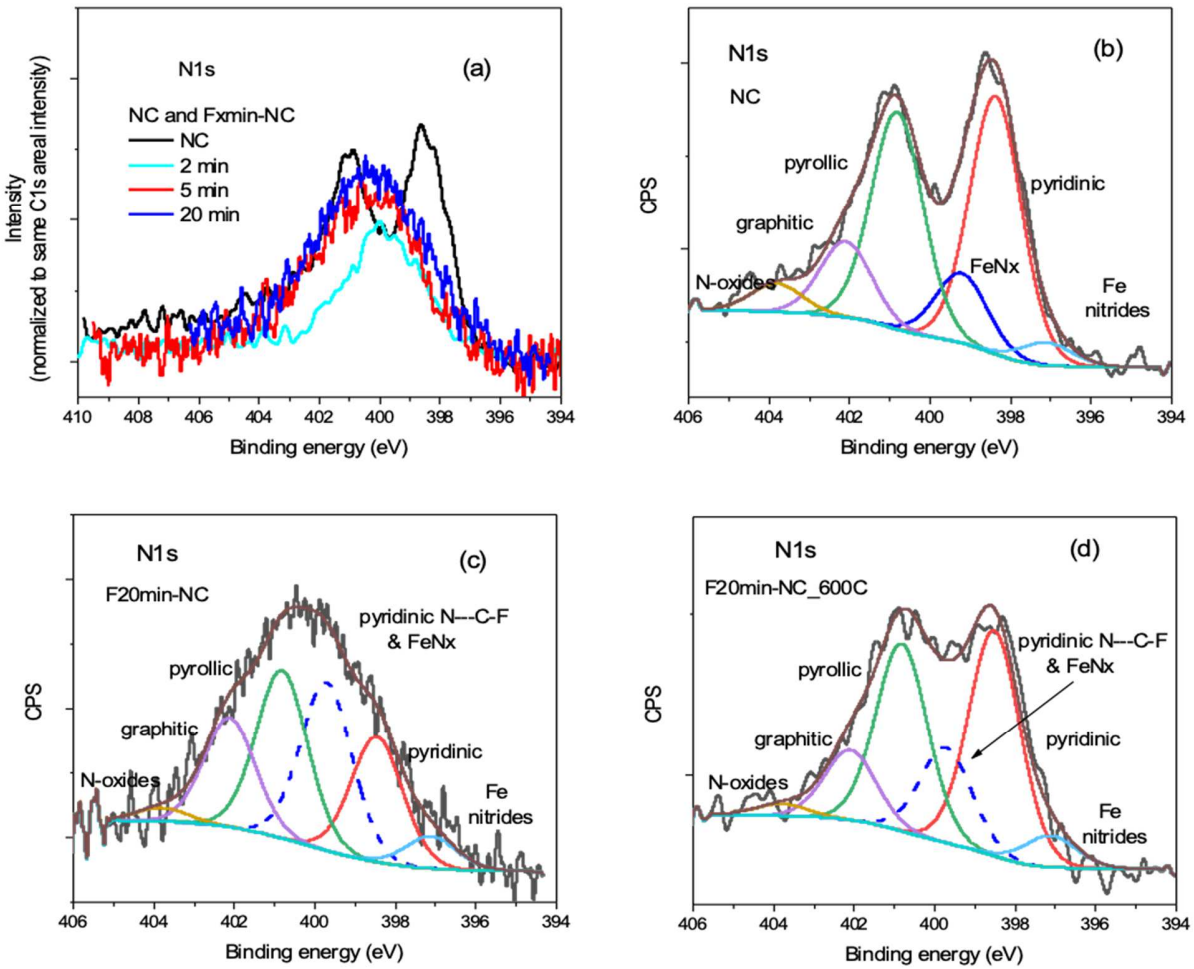

Figure 11: Deconvolutions of the N1s XPS spectra for NC series.

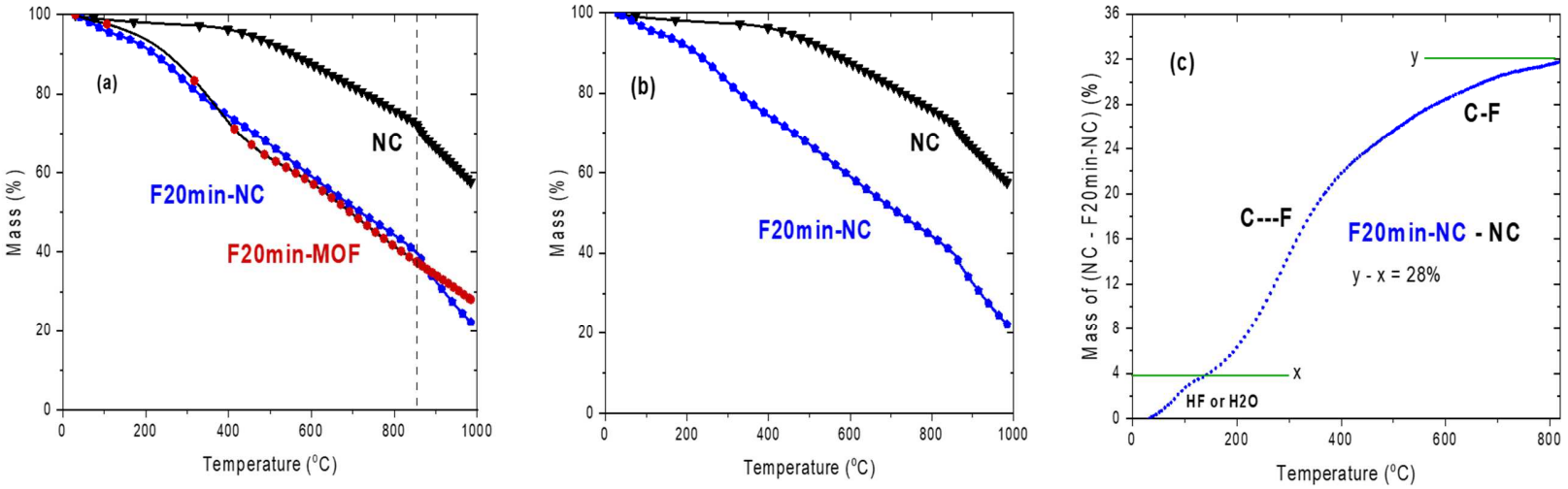

Figure 12: TGA curves of: NC, F20min-NC and F20min-MF (a); NC and F20min-NC (b); and Mass difference vs temperature between F20min-NC and NC (c).

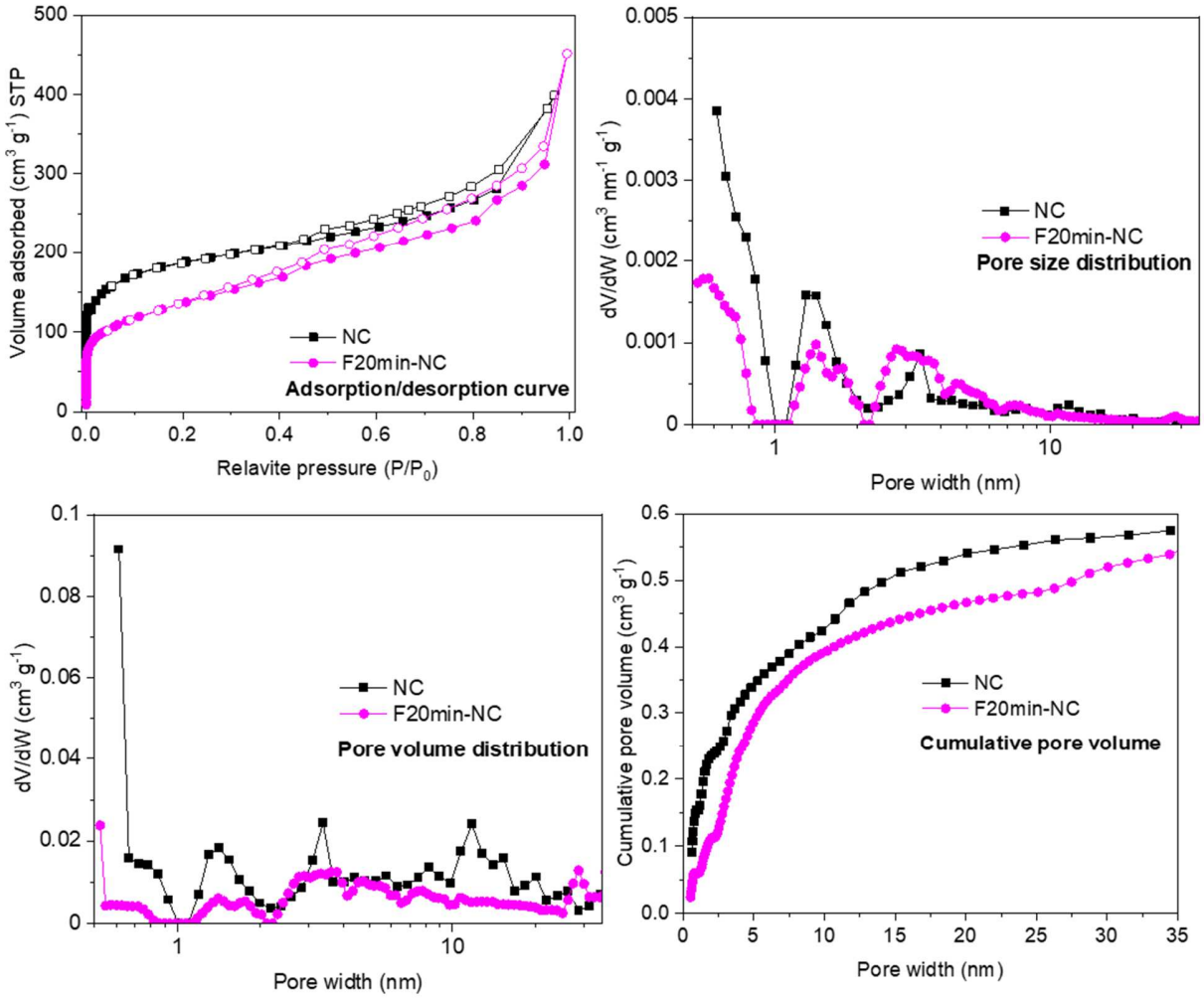

Figure 13: N_2 adsorption/desorption isotherms of NC and F20min-NC.

Table 1 : XPS and solid state NMR quantification

Sample	XPS (at%)						F/C[c]	
	C	**O**	**N**	**F**	**Fe**	**Zn**	**XPS**	**NMR**
BP	98.6	1.4	-	-	-	-	-	-
F10min-BP	93.1	3.6	-	3.4	-	-	0.04	0.05
F20min-BP	85.4	4.6	-	10.1	-	-	0.12	0.12
F1h-BP	79.5	4.2	-	16.3	-	-	0.21	0.24
F12h-BP	69.2	3.0	-	27.8	-	-	0.40	0.35
BP-N	93.6	5.6	0.8	-	-	-	-	-
F20min-BP-N	86.1	2.7	0.8	10.4	-	-	0.12	0.10
F1h-BP-N	68.1	2.5	0.7	28.7	-	-	0.42	0.30
MOF	89.9	2.7	6.5	-	-	0.9	-	-
F20min-MOF	60.6	3.9	4.8	30.2	-	0.5	0.50	0.36
NC	91.6	3.0	4.8	-	0.6	-	-	-
F2min-NC	75.5	7.2	3.2	13.0	1.1	-	0.17	0.05 (by weight)
F5min-NC	67.3	5.5	2.7	23.4	1.1	-	0.35	0.10
F20min-NC	64.6	5.2	3.3	26.0	0.9	-	0.40	0.27
F20min-NC_600	86.3	5.1	3.6	4.4	0.6	-		

Table 2 : Porosity of the various carbons used in this work before and after their fluorination at room temperature. For fluorinated samples, the values are calculated for equivalent carbon mass (i.e. corrected for the presence of fluorine).

Sample	F/C		Porosity ($m^2 g^{-1}$)			
	XPS	NMR	BET	Micropores	Mesopores	Micropores + mesopores
BP	-	-	1361	1039	276	1315
F10min-BP	0.04	0.05	1319	967	282	1249
F20min-BP	0.12	0.12	893	645	197	842
F1h-BP	0.21	0.24	726	480	184	664
F12h-BP	0.40	0.35	668	394	170	564
BP-N	-	-	1708	549	678	1227
F20min-BP-N	0.12	0.10	1165	464	536	1000
F1h-BP-N	0.42	0.30	866	261	400	661
MOF	-	-	1066	1059	42	1101
F20min-MOF	0.50	0.36	437	384	42	426
NC	-	-	976	947	155	1102
F2min-NC	0.17	0.05 (by weight)	457	497	59	556
F5min-NC	0.35	0.10	544	405	147	552
F20min-NC	0.40	0.27	472	284	150	434
F20min-NC-600			858	597	223	819

Table 3 : Relative and absolute fluorine contents for the five deconvoluted peaks of the F1s XPS spectra recorded for fluorinated BP, N-BP and MOF

	F10min-BP		**F20min-BP**		**F1h-BP**		**F12h-BP**		**F20min-BP-N**		**F1h-BP-N**		**F20min-MOF**	
Peak name	Relative cont. (%)	**Absolute cont. (at%)**	Relative cont. (%)	**Absolute cont. (at%)**	Relative cont. (%)	**Absolute cont. (at%)**	Relative cont. (%)	**Absolute cont. (at%)**	Relative cont. (%)	**Absolute cont. (at%)**	Relative cont. (%)	**Absolute cont. (at%)**	Relative cont. (%)	**Absolute cont. (at%)**
C---F	78.5	**2.7**	86.1	**8.7**	86.8	**14.2**	86.5	**24.1**	81.0	**8.4**	76.4	**21.9**	56.4	**17.0**
C-F	8.6	**0.3**	9.5	**1.0**	7.8	**1.3**	9.2	**2.6**	11.3	**1.2**	19.9	**5.7**	30.2	**9.1**
C-F_2	2.9	**0.1**	0.0	**0.0**	0.7	**0.1**	0.7	**0.2**	0.2	**0.0**	0.0	**0.0**	5.4	**1.6**
M-F_2	9.1	**0.3**	2.8	**0.3**	4.3	**0.7**	3.3	**0.9**	5.4	**0.6**	2.9	**0.8**	7.5	**2.3**
M-F	0.9	**0.0**	1.6	**0.2**	0.3	**0.1**	0.3	**0.1**	2.1	**0.2**	0.9	**0.2**	0.5	**0.1**
F	100.0	**3.4**	100.0	**10.1**	100.0	**16.3**	100.0	**27.8**	100.0	**10.4**	100.0	**28.7**	100.0	**30.2**

Table 4 : Relative and absolute fluorine contents for the five deconvoluted peaks of the F1s XPS spectra recorded for fluorinated NC catalysts before and after a heat-treatment at 600 °C under Ar.

	F2min-NC		**F5min-NC**		**F20min-NC**		**F20min-NC_600**	
Peak name	Relative cont. (%)	**Absolute cont. (at%)**	Relative cont. (%)	**Absolute cont. (at%)**	Relative cont. (%)	**Absolute cont. (at%)**	Relative cont. (%)	**Absolute cont. (at%)**
C---F	67.3	**8.7**	51.7	**12.1**	59.9	**15.6**	65.1	**2.9**
C-F	5.4	**0.7**	22.5	**5.3**	23.5	**6.1**	3.9	**0.2**
C-F_2	0.0	**0.0**	7.0	**1.6**	3.0	**0.8**	3.6	**0.2**
M/Fe-F_2	16.7	**2.2**	13.8	**3.2**	11.0	**2.9**	13.0	**0.6**
M/Fe-F	10.6	**1.4**	5.1	**1.2**	2.6	**0.7**	14.4	**0.6**
F	100.0	**13.0**	100.0	**23.4**	100.0	**26.0**	100.0	**4.4**

Table 5 : Relative and absolute carbon contents for the six deconvoluted peaks of the C1s XPS spectra recorded for unfluorinated and fluorinated N-doped carbons

		BP		**F10min-BP**		**F20min-BP**	
Peak name	Assigment	Relative content (%)	**Absolute content (at%)**	Relative content (%)	**Absolute content (at%)**	Relative content (%)	**Absolute content (at%)**
C1	undamaged C	71.5	**70.5**	68.1	**62.2**	59.1	**50.5**
C2	damaged AC or C-OH / **C-C-F**	14.2	**14.0**	14.3	**13.0**	16.7	**14.3**
C3	Csp^3 free radical defect or C=O / **C---F**	5.6	**5.6**	6.9	**6.3**	12.9	**11.1**
C4	COOH / **C-F** or **CF_2**	2.7	**2.7**	4.2	**3.9**	5.3	**4.5**
C5	$\pi^* \leftarrow \pi$ shake up satellite	6.0	**5.9**	6.5	**6.0**	5.9	**5.1**
C1s		100.0	**98.6**	100.0	**91.3**	100.0	**85.4**

	BP-N		**F20min-BP-N**		**MOF**		**F20min-MOF**		**NC**		**F20min-NC**	
Peak name	Relative content (%)	**Absolute content (at%)**	Relative content (%)	**Absolute content (at%)**	Relative content (%)	**Absolute content (at%)**	Relative content (%)	**Absolute content (at%)**	Relative content (%)	**Absolute content (at%)**	Relative content (%)	**Absolute content (at%)**
C1	61.5	**57.5**	61.0	**52.6**	34.7	**31.2**	23.0	**14.0**	62.0	**56.7**	32.7	**21.1**
C2	24.7	**23.1**	16.1	**13.8**	25.0	**22.5**	27.7	**16.8**	16.8	**15.4**	24.3	**15.7**
C3	6.6	**6.1**	12.4	**10.6**	34.8	**31.3**	27.0	**16.3**	11.3	**10.4**	25.0	**16.1**
C4	3.1	**2.9**	4.9	**4.2**	3.9	**3.5**	17.3	**10.5**	5.0	**4.6**	13.1	**8.5**
C5	4.1	**3.9**	5.7	**4.9**	1.6	**1.4**	5.1	**3.1**	3.5	**3.2**	4.9	**3.2**
C6	-	**-**	-	**-**	-	**-**	-	**-**	1.4	**1.3**	0.0	**0.0**
C1s	100.0	**93.6**	100.0	**86.1**	100.0	**89.9**	100.0	**60.6**	100.0	**91.6**	100.0	**64.6**

Table 6: Relative, absolute nitrogen contents, and nitrogen absolute contents normalized to their respective C-contents (C-norm absolute contents)* for the deconvoluted peaks of the N1s XPS spectra recorded for unfluorinated and fluorinated MOF and NC catalysts.**

	MOF		F20min-MOF			NC		F20min-NC		
Peak name	Relative content (%)	**Absolute content (at%)**	Relative content (%)	**Absolute content (at%)**	*C-norm. absolute content (at%)*	Relative content (%)	**Absolute content (at%)**	Relative content (%)	**Absolute content (at%)**	*C-norm. absolute content (at%)*
Pyridinic	55.5	**3.6**	18.7	**0.9**	*1.3*	38.4	**1.9**	20.31	**0.6**	*0.9*
Pyridinic--C-F	-	**-**	27.2	**1.3**	*1.9*	-	**-**			
Fm-FeNx with m=0, 1, 2	-	**-**	-	**-**	-	10.4	**0.5**	27.34	**0.9**	*1.3*
Pyrrolic	31.9	**2.1**	32.8	**1.6**	*2.4*	32.4	**1.6**	27.25	**0.9**	*1.3*
Graphitic	9.3	**0.6**	18.3	**0.9**	*1.3*	11.2	**0.5**	17.75	**0.6**	*0.9*
Noxide	3.3	**0.2**	3.0	**0.1**	*0.1*	4.2	**0.2**	2.21	**0.1**	*0.1*
Fe-nitrides	-	**-**	-	**-**	-	3.4	**0.2**	5.14	**0.2**	*0.2*
Total N1s	100.0	**6.5**	100.0	**4.8**	*7.0*	100.0	**4.9**	**100.0**	**3.3**	***4.7***

*Example of calculation for *C-norm absolute content* for the Total N1s of F20min-NC: 3.3 x (91.6/ 64.6) = 4.7 at%, where 3.3 is the Absolute content of N1s for F20min-NC (see Tab. 1) and (91.6 / 64.6) is the ratio of the absolute C1s contents for NC and F20min-NC (see Tab.1 for both), respectively. The C-norm absolute contents of MOF and NC are of course their respective Absolute contents.

**Due to their very low N-content (see Tab. 1), the N1s XPS spectra of BP-N samples could not be deconvoluted.

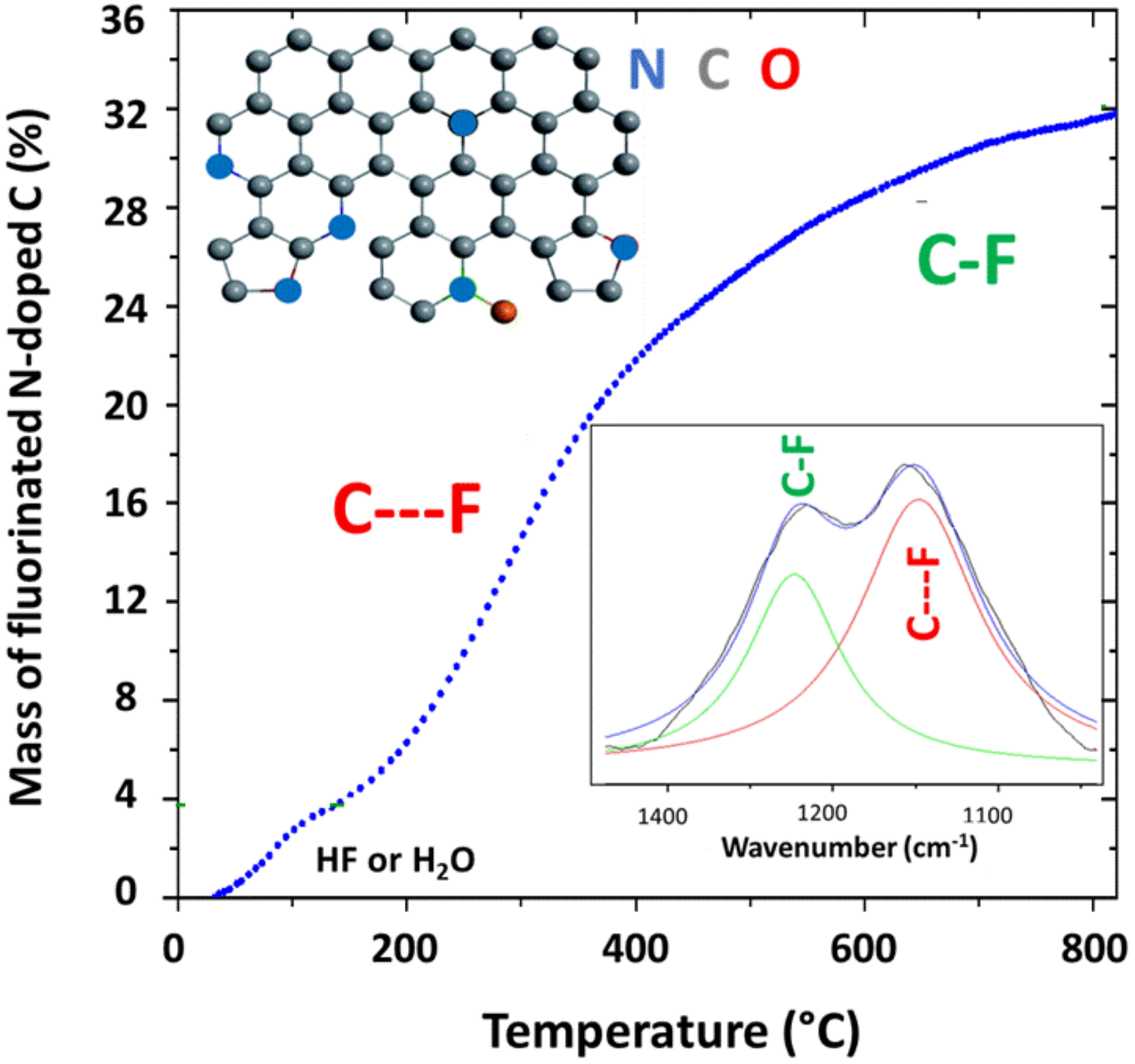
Mass of fluorinated N-doped C (%)
Temperature (°C)
0
4
8
12
16
20
24
28
32
36
0
200
400
600
800
N C O
C-F
C---F
HF or H_2O
C-F
C---F
1400
1200
1100
Wavenumber (cm^{-1})